applied sciences

MDPI

Article

In-Field Load Acquisitions on a Variable Chamber Round Baler Using Instrumented Hub Carriers and a Dynamometric Towing Pin

Filippo Coppola [1], Andrea Ruffin [2] and Giovanni Meneghetti [1,*]

[1] Department of Industrial Engineering, University of Padova, Via Venezia 1, 35131 Padova, Italy; filippo.coppola@phd.unipd.it
[2] Maschio Gaspardo S.p.A., Via Marcello 73, 35011 Padova, Italy; aruffin@maschiogaspardo.com
* Correspondence: giovanni.meneghetti@unipd.it; Tel.: +39-049-8276751; Fax: +39-049-8276785

Abstract

In this work, the load spectra acting in the vertical direction on the hub carriers and in the horizontal longitudinal direction on the drawbar of a trailed variable chamber round baler were evaluated. To this end, each hub carrier was instrumented with appropriately calibrated strain gauge bridges. Similarly, the baler was equipped with a dynamometric towing pin, instrumented with strain gauge sensors and calibrated in the laboratory, which replaced the original pin connecting the baler and the tractor during the in-field load acquisitions. In both cases, the calibration tests returned the relationship between applied forces and output signals of the strain gauge bridges. Multiple in-field load acquisitions were carried out under typical maneuvers and operating conditions. The synchronous acquisition of a video via an onboard camera and Global Positioning System (GPS) signal allowed to observe the behaviour of the baler in correspondence of particular trends of the vertical and horizontal loads and to point out the most demanding maneuver in view of the fatigue resistance of the baler. Finally, through the application of a rainflow cycle counting algorithm according to ASTM E1049-85, the load spectrum for each maneuver was derived.

Keywords: agricultural machinery; instrumentation; strain gauges; in-field loads; load spectra

Academic Editor: Roberto Romaniello

Received: 9 July 2025
Revised: 27 July 2025
Accepted: 28 July 2025
Published: 1 August 2025

Citation: Coppola, F.; Ruffin, A.; Meneghetti, G. In-Field Load Acquisitions on a Variable Chamber Round Baler Using Instrumented Hub Carriers and a Dynamometric Towing Pin. *Appl. Sci.* **2025**, *15*, 8579. https://doi.org/10.3390/app15158579

1. Introduction

Fuel consumption represents one of the main costs for agricultural companies [1–3]. Being able to measure the external loads to which an agricultural machine is subjected during usage may contribute to avoid unnecessary over-sizing and, consequently, to reduce fuel consumption. Many authors have used commercial load cells to measure the external loads of agricultural machinery [4–8]. Other authors used properly calibrated strain gauge bridges to correlate the measured strains to the applied forces [9–24]. Szusta et al. [25] determined the operational loads during a grass-cutting process on a green harvesting machine using strain gauges placed in stress concentration regions. Khan et al. [26] developed an instrumented connection between the tractor and agricultural equipment that was capable of measuring draught and vertical forces up to 20 kN. The system showed high linearity between the output of the strain gauges and the applied forces. Kostić et al. [27] developed a three-point hitch equipped with a force transducer to measure the horizontal towing loads between the tractor and the driven agricultural implement during soil tillage operations. The authors measured towing loads up to 16.0 kN and 19.9 kN on partially tilled and untilled fields, respectively. Some investigations focused on the loads acting on

the bearings of the tractor's Power Take-off (PTO) [28–30]. In particular, Hensh at al. [30] developed an octagonal ring dynamometer [31], consisting of eight strain gauges connected to form two complete Wheatstone bridges, and measured the axial and radial loads acting on the outer-side ball bearing supporting the PTO shaft. A dedicated PTO shaft for acquisitions was designed. The authors demonstrated that the depth of soil tillage, the size of the agricultural implement wheels, and the PTO transmission ratio settings influenced both the radial and axial loads acting on the bearing. Lee et al. [32] measured the PTO torque using strain gauges during soil tillage and baling operations at different tractor ground speeds and PTO rotation speeds. During the acquisitions, a 75 kW L7040 tractor by LS Mtron Ltd. was used. The Authors demonstrated that the load on the PTO is greater during soil tillage operations and that the PTO rotation speed has a greater impact on the required torque compared to the tractor speed. Similar results were found during soil tillage operations with a rotary tiller [33,34]. Shao et al. [35] obtained the load spectra during operation of the rear axle of a dump truck using strain gauges. Moreover, the accumulated damage in operation was calculated according to the Palmgren–Miner hypothesis [36–38]. Similar fatigue monitoring [39] investigations were carried out on railway axles [40], truck crane jib structures [41], and bogie frames of railway trains [42]. In particular, Maglio et al. [40] measured the bending stress spectra of railway axles using an instrumented powered wheelset over a 22-month period, while Dong et al. [41] and Wang et al. [42] derived the load or stress spectra from smaller sample data collected over shorter periods: 30 days in Dong et al.'s [41] case, and approximately 3.5 h in Wang et al.'s study [42]. In all three above-mentioned investigations, the fatigue life assessment was also reported.

In the present investigation, the load spectra acting in the vertical direction on the hub carriers and in the horizontal longitudinal direction on the drawbar of a variable chamber trailed round baler were measured. To this end, a 3940 kg baler was equipped with a specially designed dynamometric towing pin used to measure the horizontal loads acting on the drawbar of the baler during in-field load acquisitions. Furthermore, the hub carriers of the baler were instrumented with properly calibrated full bridge channels in order to measure the vertical loads on each hub carrier. To define the strain gauge arrangement, linear elastic finite element analyses were carried out on the right hub carrier in Ansys software environment to achieve the appropriate sensitivity of the measuring system, according to widely adopted design methods to assess stress distributions in agricultural equipment [7,23,35]. Five different maneuvers were performed to measure the loads acting both under normal operating conditions and during extreme events. During each maneuver, any noteworthy trends in the time variant loads were described and the corresponding events identified. This was possible by means of the synchronous acquisition of the signals coming from an onboard camera and a GPS. Afterwards, the load spectra for each maneuver were obtained according to ASTM E1049-85 standard [43]. Understanding the magnitude and origin of these external loads linked to specific operating maneuvers provides essential input for engineers involved in the design, development, and target lifetime assessment of similar agricultural implements.

2. Research Methodology

2.1. Description

The experimental setup used for measuring the external vertical loads $F_v(t)$ acting on the hub carriers of the trailed round baler under investigation is reported in Figure 1. Both left (L) and right (R) hub carriers were instrumented with two 0°/90° strain gauge rosettes wired in a full-bridge configuration. In particular, each hub carrier was equipped with two HBM K-CXY31-3/120 [44] strain gauge rosettes matched to steel (0°/90°, grid length 3 mm, linear thermal expansion coefficient 10.8 × 10^{-6}/°C) placed on the two

ribs strengthening the hub carrier structure. The full-bridge configuration allowed to automatically compensate for temperature changes during in-field load acquisitions [45]. The strain gauge rosettes were installed at the point of highest sensitivity of the strain gauge bridge, which was evaluated through a Finite Element (FE) analysis using Ansys Workbench R22 [46]. In particular, linear elastic FE analyses were carried out using 8-node linear hexahedral SOLID 185 elements. As the hub carriers were made of S275 structural steel material, a Young's modulus and Poisson's ratio of 206 GPa and 0.3, respectively, were adopted, as recommended by international standards [47,48]. The hub carrier welds were not modelled. Finally, constraints were set to replicate the bolted connection between the hub carrier and the main frame of the round baler, while a remote force simulating a vertical load transmitted from the ground to the hub carrier, considering a 550/45-22.5 trailer tyre, was applied. The FE model is visible in Figure 2.

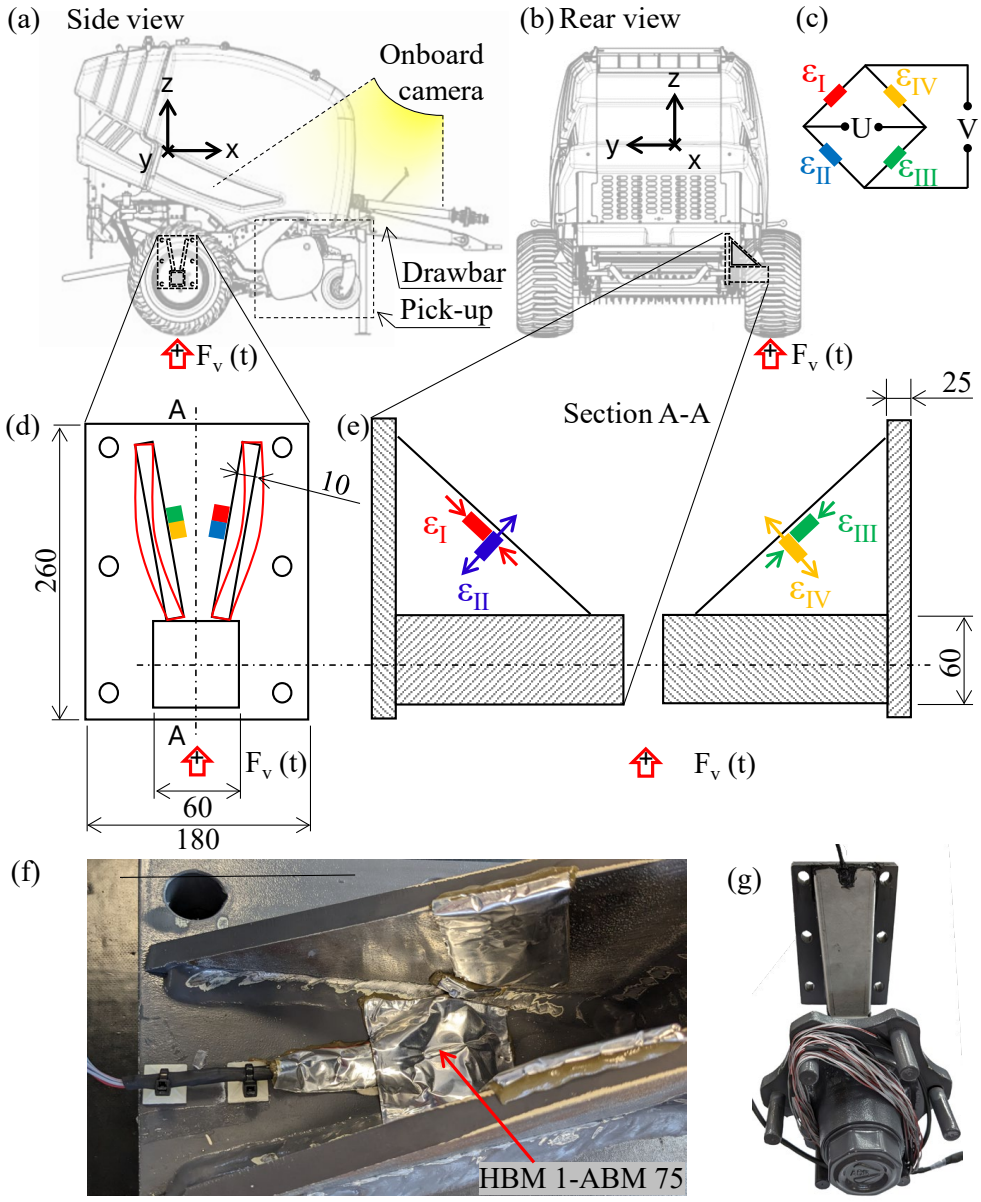

Figure 1. (**a**–**e**) The right hub carrier instrumented with two strain gauge rosettes wired in a full-bridge configuration, (**f**,**g**) instrumented right hub carrier (dimensions in mm).

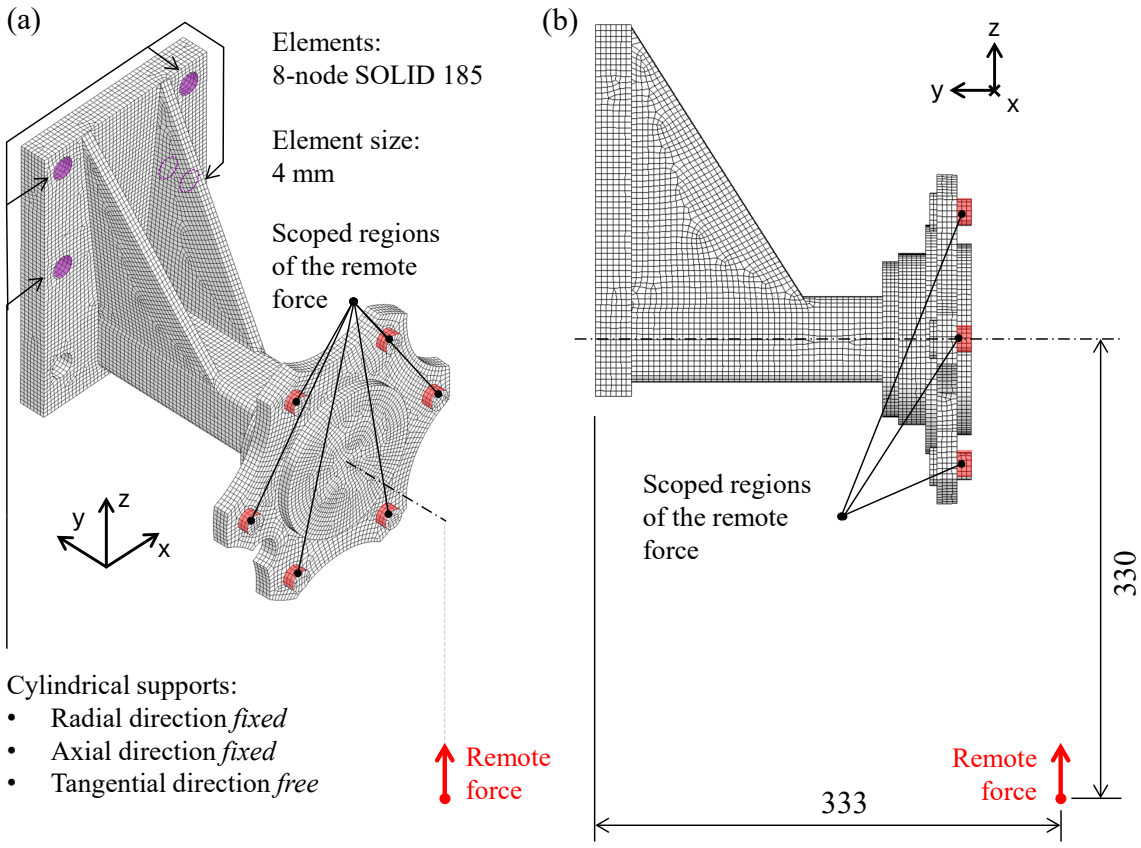

Figure 2. FE model of the R hub carrier: (**a**) isometric view and (**b**) rear view.

The full Wheatstone bridge (Figure 1c) is governed by the following equation:

$$\frac{U}{V} = \frac{K}{4}(\varepsilon_I - \varepsilon_{II} + \varepsilon_{III} - \varepsilon_{IV}) = \frac{K}{4}\cdot 2(1+\nu)\cdot\varepsilon_I = \frac{K}{4}\cdot N\cdot\varepsilon_I \quad (1)$$

where U (≈mV) is the output signal, V is the supply tension (5 V), K is the gauge factor equal to 2.07, ν the Poisson's ratio of S275 steel material equal to 0.3 and N is the bridge factor equal to 2·(1 + ν), according to the arrangement reported in Figure 1.

Similarly, Figure 3 shows the experimental setup used to measure the horizontal loads $F_h(t)$ acting on the round baler's drawbar. The drawbar is highlighted in Figure 1a. A specifically designed towing system, which replaced the original connection between the baler and the tractor during in-field loads acquisitions, was adopted and is presented in Figure 3a, with its dynamometric body being the towing pin (Figure 3b,c). The dynamometric towing pin was made of 39NiCrMo3 alloy steel and had a nominal diameter of 20 mm, with the exception of the central portion that contacts the baler's eyelet, where the diameter was increased to 28 mm. Changing the diameter allowed to maintain the original clearances between the eyelet and the pin while increasing the sensitivity of the measuring system. Finally, it is worth noting that undesired translations and rotations of the dynamometric towing pin around its longitudinal axis were prevented by means of a locking plate placed on top of the wishbone (Figure 3a). Attention was paid to design a locking plate that would not affect the deformations of the dynamometric towing pin during usage.

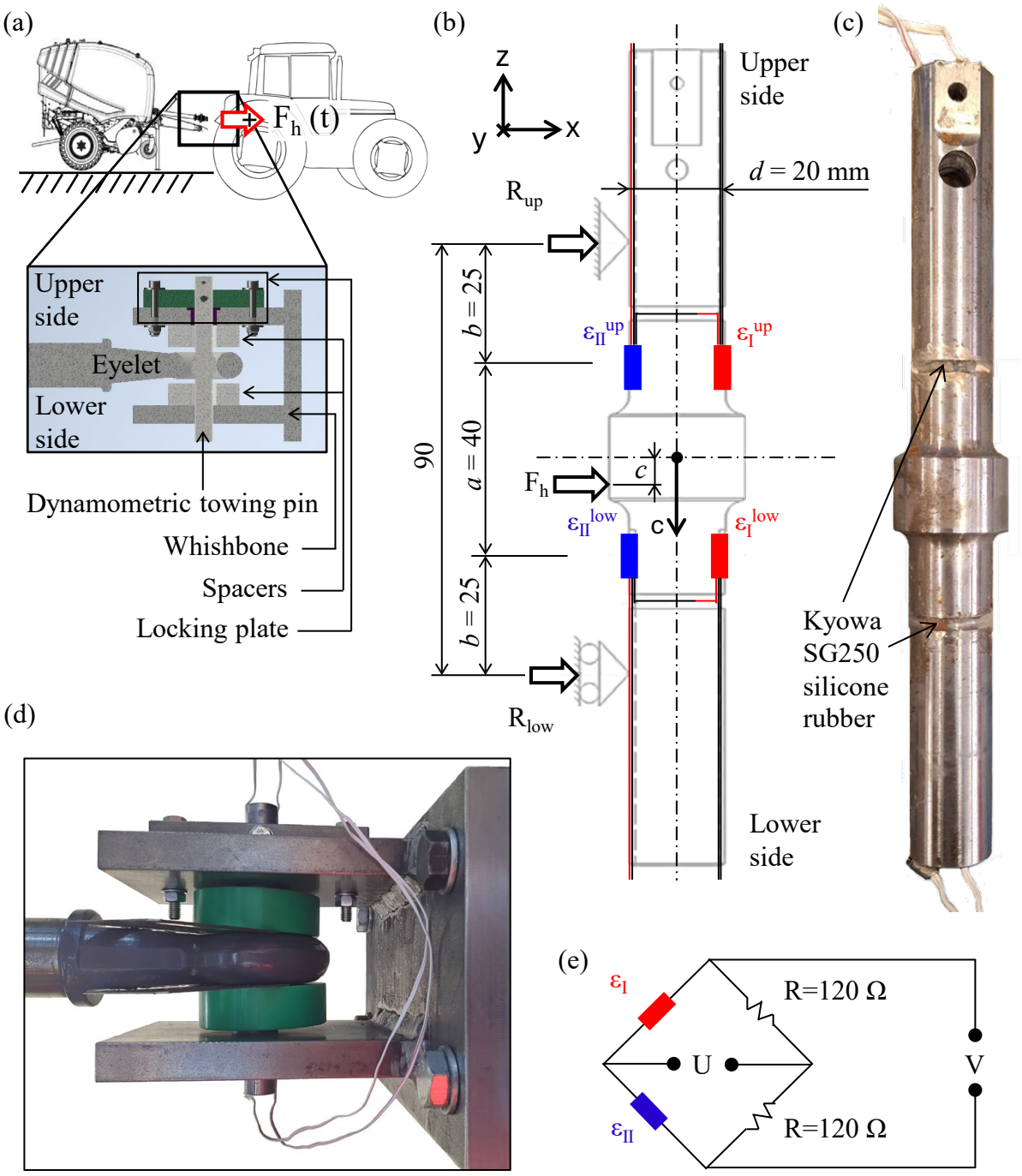

Figure 3. (**a**,**b**) Experimental setup used to acquire the horizontal loads $F_h(t)$ acting on the round baler's drawbar, (**c**,**d**) instrumented dynamometric towing pin and (**e**) schematisation of the adopted half Wheatstone bridges.

Figure 3b reports the adopted strain gauge configuration. In particular, four Kyowa KFGS-3-120-C1-11 [49] strain gauges matched to steel (uniaxial, grid length 3 mm, linear thermal expansion coefficient 11.7 × 10^{-6}/°C) were applied to the towing pin in dedicated milled grooves and connected to form two half-bridges (Figure 3e) on the upper and lower sides of the dynamometric towing pin, respectively, according to the half Wheatstone bridge Equation (2):

$$\frac{U}{V} = \frac{K}{4}(\varepsilon_I - \varepsilon_{II}) = \frac{K}{4} \cdot 2 \cdot \varepsilon_I = \frac{K}{4} \cdot N \cdot \varepsilon_I \quad (2)$$

where $\varepsilon_I = -\varepsilon_{II}$ and the gauge factor K and bridge factor N were set equal to 2.11 and 2, respectively. The half-bridge configuration allowed to automatically compensate for temperature changes during in-field load acquisitions [45]. By doing so, it was possible to compute the horizontal loads F_h acting on the drawbar of the round baler as the sum of the reaction forces R_{up} and R_{low} (Figure 3b) obtained by means of Equations (3) and (4) of solid mechanics, respectively.

$$R_{up} = \frac{E \cdot \varepsilon_I^{up} \cdot W}{b} \quad (3)$$

$$R_{low} = \frac{E \cdot \varepsilon_I^{low} \cdot W}{b} \quad (4)$$

$$F_h = R_{up} + R_{low} \quad (5)$$

In Equations (3) and (4), $W = \pi \cdot d^3/32$ is the section modulus evaluated analytically, considering a constant diameter of the towing pin equal to 20 mm, while E is Young's modulus of the adopted steel material and was assumed to be equal to 206 GPa.

2.2. Calibration

Figure 4a presents a schematisation of the adopted calibration procedure along with the signal acquired at the L hub carrier during one of the three monotonic load ramps executed. Specifically, two digital scales and an overhead crane to lift the baler were used. Initially, the full-bridge channels were balanced (i.e., zeroed) with no load applied to the hub carriers (i.e., the baler was fully lifted by the overhead crane and without the wheels attached to the hub carriers), and then three experimental points were acquired for each monotonic load ramp: *(i)* the baler was fully lifted by the overhead crane (the strain gauge bridges returned $\varepsilon_I > 0$ due to the wheel weight (see Figure 1), digital scales returned 0 kN); *(ii)* the baler was partially lifted by the overhead crane (the strain gauge bridges returned $\varepsilon_I = 0$, digital scales returned the wheel weight equal to 1.24 kN); and *(iii)* the baler was not supported by the overhead crane (the strain gauge bridges returned $\varepsilon_I < 0$ (see Figure 1), left and right digital scales returned 14.2 kN and 9.10 kN, respectively). Figure 4b,c report the calibration curves obtained for the L and R hub carriers, respectively. Furthermore, in Figure 4b, c, the relationship between measured strains and the corresponding computed loads is highlighted: negative ε_I strains correspond to positive loads. Therefore, vertical loads, F_v, are considered positive when acting in the positive z direction, as illustrated in Figure 1. Finally, it is worth mentioning that the sensitivity of the strain gauge bridges to potential lateral or longitudinal loads on the L and R hub carriers was not evaluated, as these were considered negligible owing to flatness of the test field, the pre-planned in-field load acquisition maneuvers, and the use of an unbraked baler.

Figure 5 reports the experimental setup used for calibrating the dynamometric towing pin used to measure the horizontal loads $F_h(t)$ on the round baler's drawbar. A specially dedicated servo-hydraulic test bench was used to obtain the relationship between the measured strains provided by the upper and lower half bridges (i.e., $\varepsilon_{I^{up}}$ and $\varepsilon_{I^{low}}$, respectively, see Figure 3b) and the load applied to the dynamometric towing pin. To this end, a 70 kN EnginLAB servo-hydraulic actuator equipped with a 100 kN Aep TC4AMP load cell and a closed-loop digital controller EnginLAB RTC9000 were used. The role of the dynamometric towing pin stiffness during calibration was extensively investigated in the discussion accompanying the next Figures 6 and 7.

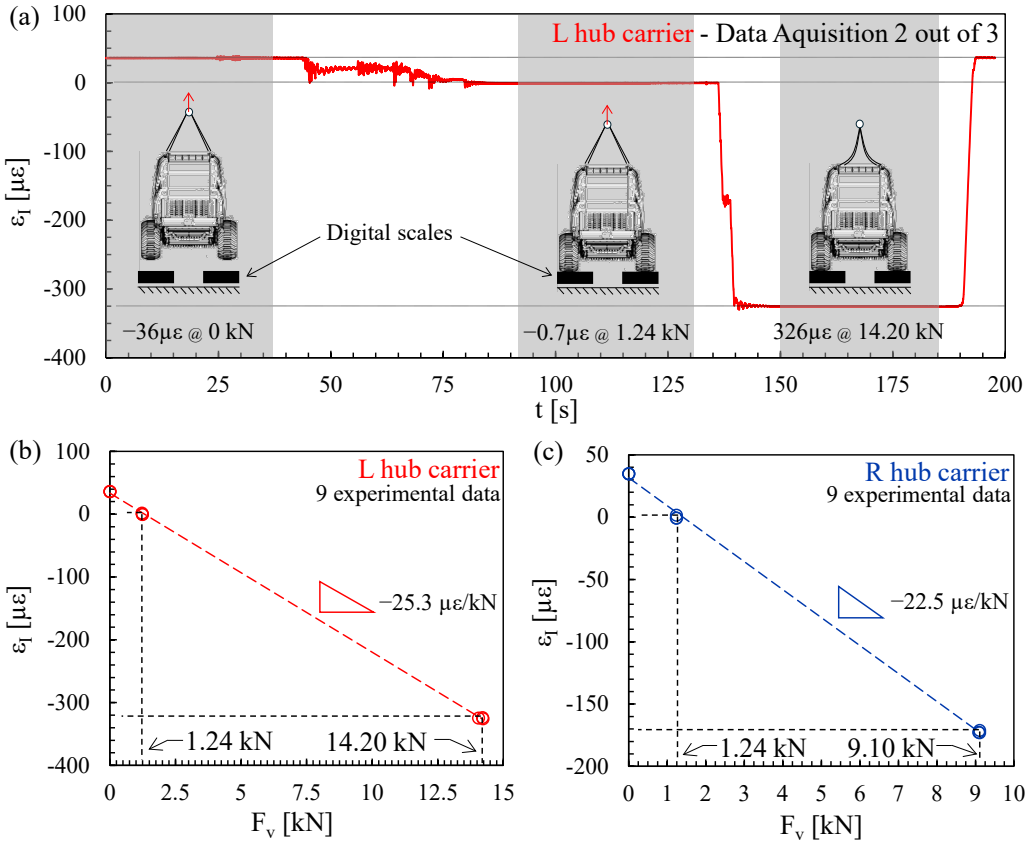

Figure 4. Calibration of the full-bridge channels at the hub carriers: (**a**) data acquisition procedure, (**b**,**c**) experimental sensitivity obtained for the L and R hub carriers, respectively.

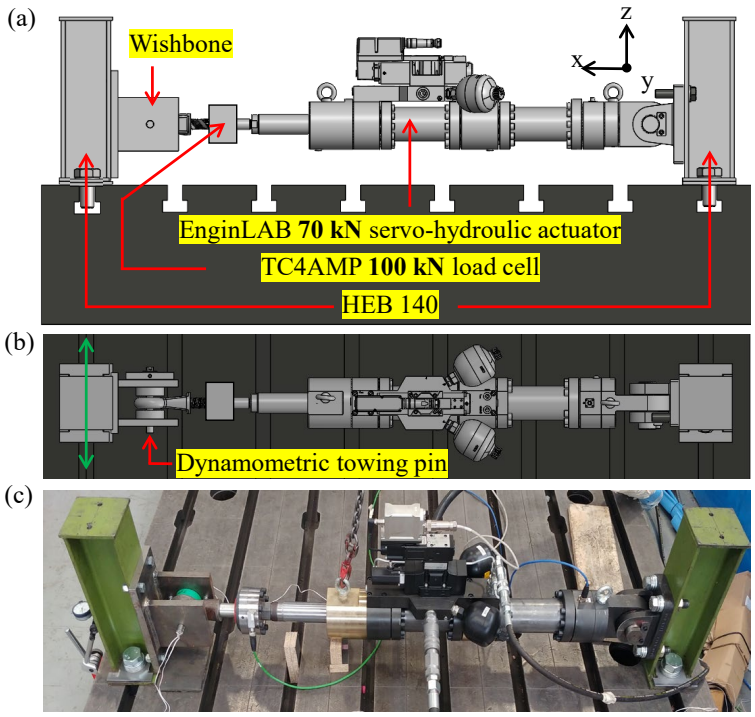

Figure 5. Servo-hydraulic test bench used for calibrating the dynamometric towing pin: (**a**) side view (**b**) upper view and (**c**) image of the experimental setup.

Figure 6 shows the relationships obtained between the strains provided by the upper and lower half bridges and the load F_{exp} applied to the dynamometric towing pin by

means of the servo-hydraulic actuator. In particular, three pulling configurations (force in the negative x direction in Figure 5a) with c = 0 mm, c = −2.0 mm, and c = 3.8 mm (c visible in Figure 3) and three pushing configurations (force in the positive x direction in Figure 5a) with c = 0 mm, c = −3.8 mm, and c = 3.8 mm were investigated. Specifically, two loading–unloading monotonic ramps were performed for each configuration. It is worth mentioning that the applied loads were such as to obtain the relationship between $\varepsilon_{I^{up,low}}$ and F_{exp} across the entire range of strains anticipated during the in-field load acquisitions. Moreover, before conducting the calibration tests, multiple loading–unloading ramps at increasing peak loads were carried out, both for pulling and pushing configurations, to investigate if residual strains were measured by the upper and lower half bridges (i.e., $\varepsilon_{I^{up}}$ and $\varepsilon_{I^{low}}$, respectively, see Figure 3b). As a result, it was possible to exclude macroscopic yielding of the dynamometric towing pin's steel material at any load level applied during the calibration tests. Figure 6 highlights the adopted sign convention: positive strains and loads act on the dynamometric towing pin during pushing (braking events), negative strains and loads act during pulling (acceleration events). When $c \neq 0$ (Figure 6c–f), the half bridge closer to the location where the load is applied returns higher absolute strains. Figure 6 also shows that the relationship between ε_I and F_{exp} is not linear in all investigated cases. The Authors interpreted this phenomenon involving the compliant behaviour of the towing pin.

In fact, the equilibrium of the towing pin can be expressed as follows:

$$\frac{R_{up}}{F_{exp}} = \frac{a/2 + b - c}{2b + a} \tag{6}$$

$$\frac{R_{low}}{F_{exp}} = \frac{a/2 + b + c}{2b + a} \tag{7}$$

where a, b, and c are reported in Figure 3b and $2b + a$ is the distance between the two reactional forces R_{up} and R_{low}.

Then, given Equations (3) and (4), Equations (6) and (7) can be re-written as follows:

$$\frac{\varepsilon_I{}^{up}}{F_{exp}} = \frac{a/2 + b - c}{2b + a} \cdot \frac{b}{W \cdot E} \tag{8}$$

$$\frac{\varepsilon_I{}^{low}}{F_{exp}} = \frac{a/2 + b + c}{2b + a} \cdot \frac{b}{W \cdot E} \tag{9}$$

Since in Equations (8) and (9) a, c, W, and E are constant, the reason for the lack of linearity of the $\varepsilon_{I^{up,low}}$ versus F_{exp} relationship was attributed to the lever arm b (Figure 3b), which reduces its effective length when the dynamometric towing pin is progressively bent in response to the applied load. Therefore, it was chosen to express the lever arm b as a function of the strains returned by the upper and lower half bridges. Since F_{exp}, $\varepsilon_{I^{up}}$, and $\varepsilon_{I^{low}}$ are given by the load cell and strain gauge readings during the calibration phase, Equations (8) and (9) can be used to express b as a function of ε_I both for the pulling and pushing configurations. By doing this, the measured horizontal loads F_h can be computed using Equations (3)–(5) and the $b = f(\varepsilon_I)$ function. The obtained results are presented in Figure 7. As previously mentioned, it is seen that the higher the strains returned by the half bridges, the lower the computed b values. After using the $b = f(\varepsilon_I)$ function, Figure 8 reports the relationship between the measured horizontal loads F_h versus the applied horizontal loads F_{exp}. Figure 8 shows that when loads exceeding ±10 kN are applied, the dynamometric towing pin returns measurements with errors not greater than ±6.5%.

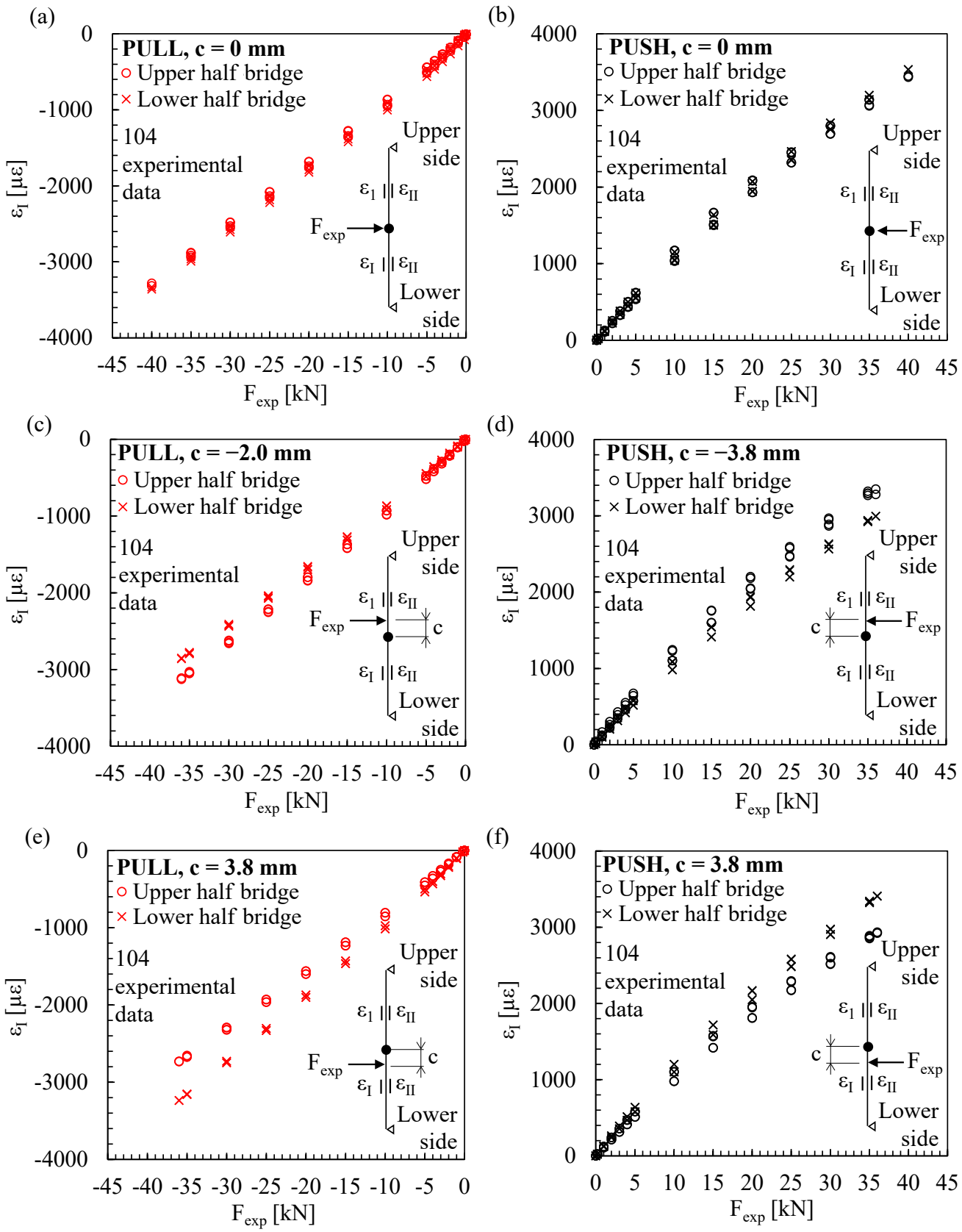

Figure 6. Experimental calibration of the dynamometric towing pin: relationships between $\varepsilon_{I\,up,low}$ strains provided by the upper and lower half bridges, respectively, and the applied load F_{exp} for (**a**,**c**,**e**) pulling configurations and (**b**,**d**,**f**) pushing configurations.

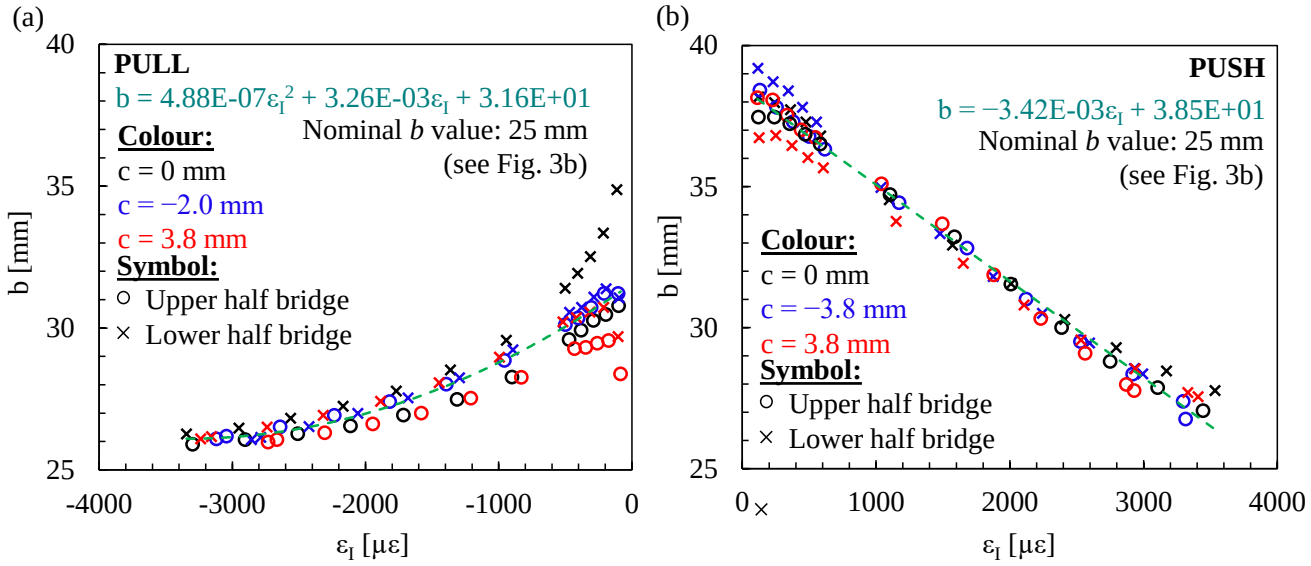

Figure 7. Experimental relationships between the $\varepsilon_{I^{up,low}}$ strains returned by the upper and lower half bridges and the lever arm *b*: (**a**) pulling configurations, (**b**) pushing configurations.

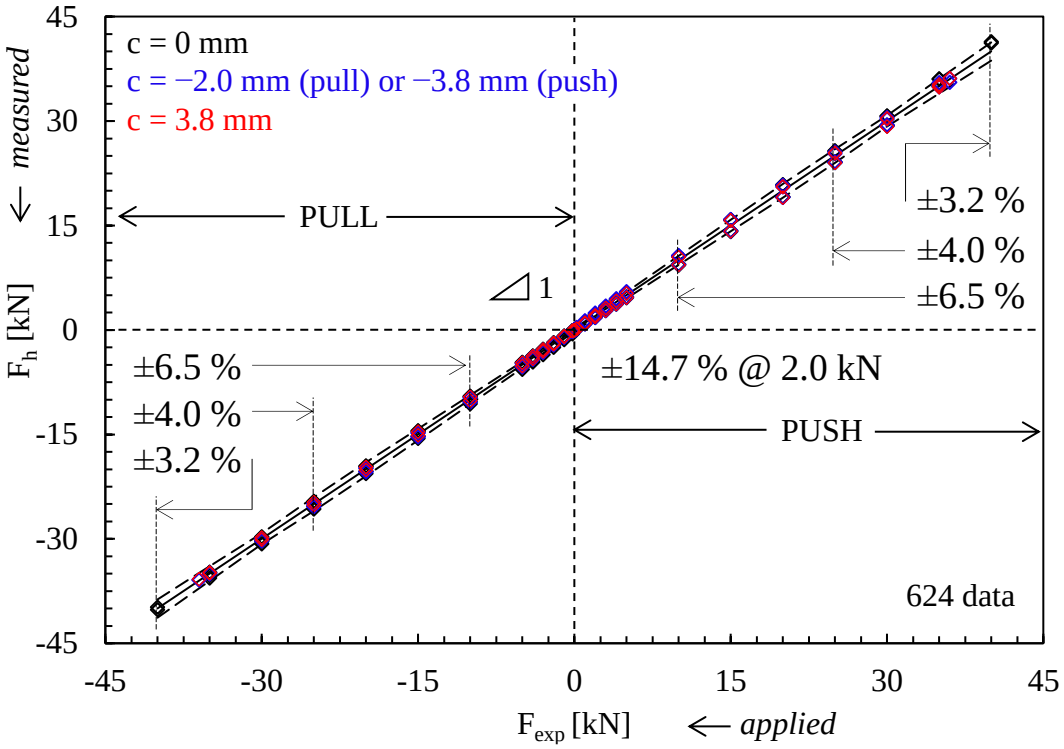

Figure 8. Relationship between the horizontal loads F_h measured by the strain gauge channels versus the horizontal loads F_{exp} applied by the servo-hydraulic actuator.

2.3. Testing of the System

Table 1 reports the maneuvers performed, the number of acquisitions carried out for each maneuver, and the total duration of the acquisitions, where any downtime was excluded. The baler settings are presented in Table 2, where the baler and PTO rotation speeds can be seen along with the blade settings and the desired bale diameter. Retracting the blades allowed to reach higher baler speeds, while the desired bale diameter was set to its maximum to achieve the heaviest possible bale.

Table 1. Acquisitions schedule.

Maneuver	n° of Acquisitions Carried out	Total Duration [s]
Product collection	7	2331
Acceleration and emergency braking with a loaded baler	2	32
Acceleration and emergency braking with an empty baler	1	16
High-speed running perpendicular to the sowing lines	1	21
Road transportation	1	895

The acquisitions were carried out with a variable chamber round baler having an unladen weight of 3940 kg, and were performed during the summer in a field located in northeastern Italy. The harvested product was corn stalks. The *product collection* acquisitions were initiated with an empty baler. In each acquisition, a single round bale was collected, tied, and unloaded. The *acceleration followed by emergency braking* acquisitions, both with a loaded and an empty baler, included an initial acceleration phase up to approximately 30 km/h and a subsequent braking phase. The *high-speed running perpendicular to the sowing lines* acquisition was performed without collecting product and with an empty baler at a nominal constant speed of 12 km/h. The *road transportation* acquisition was conducted on asphalt with an empty baler, and 4.31 km were covered at an average speed of 17.3 km/h. The maximum speed reached was 34.7 km/h. It is worth mentioning that in all the above presented maneuvers, the acquisitions were started and stopped with the baler at a standstill.

Table 2. Baler settings.

Baler speed:	1–4 km/h
Blades:	retracted
Bale diameter:	1650 mm
PTO:	440 rpm

During the execution of the maneuvers, the signals coming from each hub carrier and from the dynamometric towing pin were acquired through an IMC CS-7008-FD Data Acquisition system equipped with eight analog channels (imc Test & Measurement GmbH, Berlin, Germany). The sampling frequency was set to 200 Hz, which was appropriate to capture the phenomena which the baler underwent during usage, and an anti-aliasing filter (AAF) was also activated. Additionally, video signals from a GoPro Hero 10 Black (GoPro, San Mateo, CA, USA) (1080p, 30 fps) and the instantaneous speed, latitude, and longitude coordinate signals from a Garmin GPS18x-5 Hz (Garmin, Olathe, KS, USA) (sampled at 5 Hz) were acquired. Subsequently, the obtained data were downloaded via Wi-Fi and post-processed using IMC Studio® 5.2 and IMC FAMOS® Enterprise 2023 software. Specifically, a Butterworth low-pass filter with a 15 Hz cut-off frequency was applied in the post-processing phase.

Regarding the vertical load acquisitions, prior to each acquisition session, the strain gauged channels of the hub carriers were zeroed with the baler and the tractor standing on flat asphalt. This was done because, even if the balancing procedure was already carried out during the calibration of the hub carriers' channels, it was the Authors' choice to repeat the balancing procedure every time the IMC CS-7008-FD data acquisition system was shut down. Therefore, only the sensitivity previously obtained (i.e., -25.3 $\mu\varepsilon$/kN and -22.5 $\mu\varepsilon$/kN for the L and R hub carriers, respectively) and reported in Figure 4b,c was maintained. By doing so, only the dynamic component of the in-field loads acting on the hub carriers was acquired during each acquisition. The corresponding static load

on each hub carrier due to the weight of the baler was later included during the post-processing phase by offsetting the acquired signals. The applied offsets were evaluated by means of digital scales, one under each wheel, prior to the first acquisition session and are reported in Table 3, where two different conditions are highlighted: *(i)* the product collection mechanism (pick-up) raised and *(ii)* the product collection mechanism deployed. The pick-up is visible in Figure 1 and in the next Figures 11, 16 and 17, which will be discussed later. As reported in Table 3, when the pick-up was raised, its weight was partially carried by the hub carriers, therefore returning higher offsets. Using the video recorded by the onboard camera, which framed the pick-up during the acquisitions, it was possible to select the correct offset to be applied during the different maneuvers and during the different phases of each maneuver.

Table 3. Weight distribution of the baler.

	Raised Pick-Up [kN]	Deployed Pick-Up [kN]
R hub carrier	13.79	13.36
L hub carrier	14.32	13.45

Regarding the horizontal load acquisitions, the procedure adopted for zeroing off-line the two half bridges of the dynamometric towing pin was as follows: at the beginning of each acquisition, a maneuver consisting of three slow movements was performed: *(i)* forward, *(ii)* reverse, and *(iii)* forward. By doing so, it was possible to derive the offsets to apply to the upper and lower half bridges for properly zeroing the signals in post-processing, thanks to the clearance between the towing pin and the eyelet. A sketch of the adopted off-line procedure is reported in Figure 9. The strain signal was converted into a load signal by means of Equations (3)–(5) and of the previously introduced $b = f(\varepsilon_I)$ function (Figure 7).

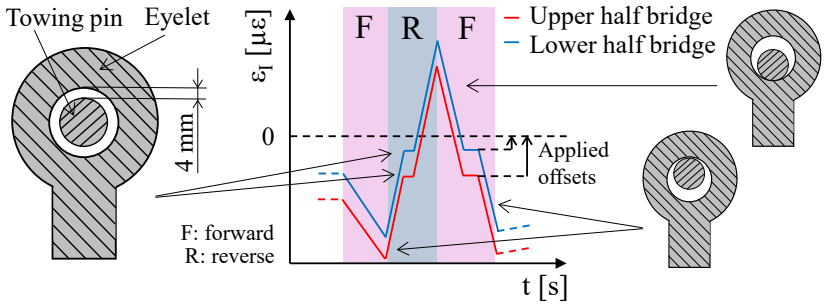

Figure 9. Sketch of the off-line procedure adopted for zeroing the signals of the dynamometric towing pin (the 4 mm clearance is highlighted).

3. Load Acquisition Results and Discussion

3.1. Load Identification

Figure 10 reports a satellite image of the two fields where the maneuvers were carried out and the routes followed by the baler, while Figure 11 shows the baler used for the in-field load acquisitions towed by a Claas Arion 660 tractor during a *product collection maneuver*. The corresponding vertical loads $F_V(t)$ on the left and right hub carriers are presented in Figure 12a. Figure 12d displays the path followed by the round baler according to the acquired GPS signal. Figure 12b,e report the vertical forces while the baler was towed to collect product along the sowing lines with the pick-up (Figure 11) deployed. In Figure 12c, the baler was towed while crossing the sowing lines with the pick-up raised (Figure 16), and no product was collected during such maneuver. It is seen that the acquired vertical forces

in Figure 12c differ significantly from those in Figure 12b,e, showing oscillations at higher amplitude and frequency. Therefore, when reporting the maximum and minimum loads acquired for each maneuver in the next Table 4, which will be commented later, the two portions of the *product collection* maneuvers reported in Figure 12c and Figure 12b and 12e, respectively, were kept distinct. In more detail, the portion where the baler moved from one swath to another (as in Figure 12c) is referred to as a *headland turning*. It is worth mentioning that the *headland turning* is present only in four out of the seven *product collection* maneuvers carried out; in the remaining three cases, the bale was collected, tied, and unloaded within the same swath.

Figure 12 highlights also that the R hub carrier channel consistently exhibited higher vertical loads compared to the L hub carrier, with the exceptions during the intervals 120 s < t < 130 s (Figure 12b), 160 s < t < 170 s (Figure 12b), and 180 s < t < 240 s (Figure 12c). In the latter interval (180 s < t < 240 s, Figure 12c), the baler was towed while running perpendicular to the sowing lines. To the Authors, the consistently higher $F_{,v,R\text{-hub carrier}}$ loads compared to the $F_{,v,L\text{-hub carrier}}$ when running parallel to the sowing lines during the product collection maneuver (Figure 12b,d) could be attributed to the influence of the sowing lines, which caused the baler to stay inclined to its right side.

Figure 12f reports the effect of the baler's rear door opening (at t = 351.3 s) on the R and L hub carriers. The baler's rear door is reported in Figure 11. Once the baler's rear door reached the fully opened position, the load on the hub carriers temporarily decreased, triggering a damped oscillation. Figure 12g reports the effect of starting the PTO (at t = 55 s) on the R hub carrier signal. The rotating parts of the baler caused small-amplitude and high-frequency loads on the hub carriers.

Figure 10. Satellite image of the fields where the load acquisitions took place; the routes followed by the baler during the different acquisitions are reported.

Figure 11. Round baler with the product collection mechanism (pick-up) deployed during the in-field load acquisitions and towed by a Claas Arion 660 tractor.

Using the dedicated fast Fourier transform (FFT) routine available in the commercial software IMC FAMOS® Enterprise 2023, the signals reported in Figure 12f, g are presented in the frequency domain in Figures 13a and 13b, respectively. Figure 13b highlights a peak at around 7.3 Hz, corresponding to the PTO rotation frequency. Another peak at around 5.5 Hz is present and is also present in Figure 13a, suggesting that it might correspond to the baler's natural frequency. A peak at the same frequency was observed also during the *road transportation* acquisitions while running on asphalt at constant speed.

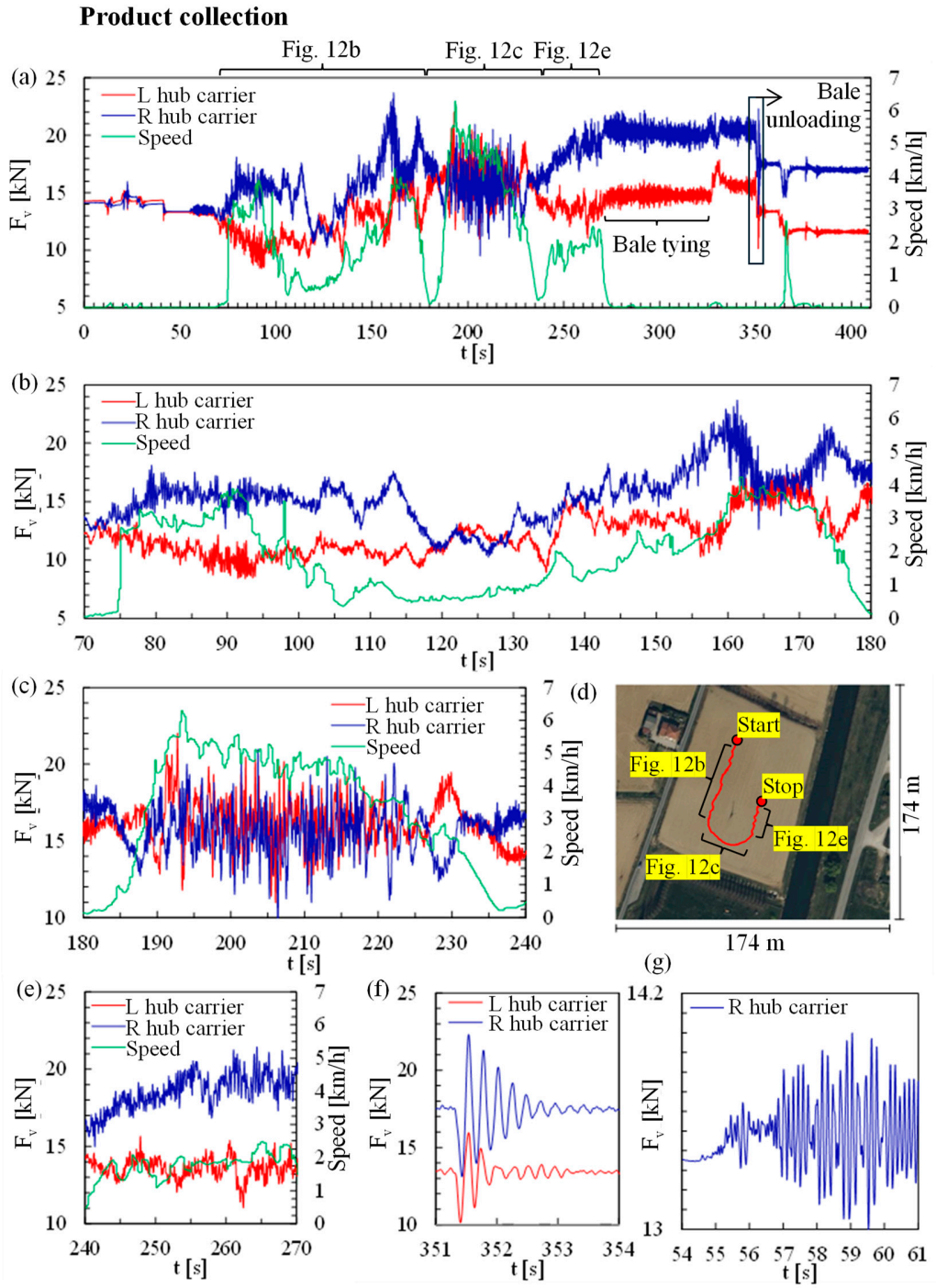

Figure 12. Vertical loads $F_V(t)$ acting on the L and R hub carriers of the round baler during a *product collection* maneuver: (**a**) whole acquisition, (**b**,**e**) product collection, (**c**) headland turning, (**d**) GPS route, (**f**) effect of the baler's rear door opening on the L and R hub carriers, and (**g**) effect of starting the PTO on the R hub carrier.

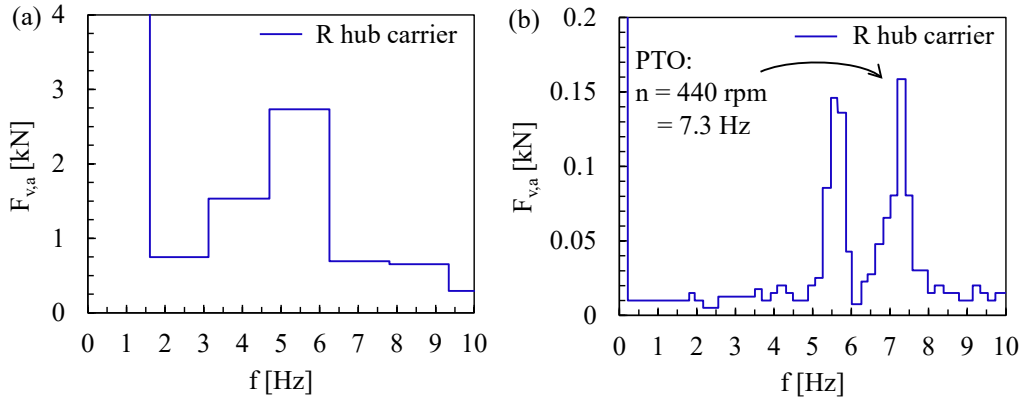

Figure 13. (**a**,**b**) R hub carrier signals from Figures 12f and 12g, respectively, presented in the frequency domain.

Figure 14a reports the horizontal loads $F_h(t)$ registered by the dynamometric towing pin during an *acceleration followed by emergency braking with a loaded baler*. The acceleration and braking phases were performed by towing the baler parallel to the sowing lines, as indicated in Figure 14b. The peak loads registered during the acceleration and braking phases were −26.6 kN and +41.5 kN, respectively. The braking phase was completed in approximately two seconds, during which the baler decelerated from 32 km/h to 0 km/h. This corresponded to an average deceleration, intended as $\Delta v/\Delta t$, of 0.45 g with an initial peak of about 0.96 g at t = 86.8 s.

Figure 15 reports the vertical loads $F_v(t)$ acquired by the L and R hub carriers while running perpendicular to the sowing lines. It is worth mentioning that the maximum and minimum loads registered by the hub carriers came from this maneuver. In particular, the R hub carrier registered a force of +38.8 kN at t = 75.4 s (indicated by a blue arrow in Figure 15b), while the L hub carrier registered a force of −4.68 kN at t = 75.8 s (indicated by a red arrow in Figure 15b).

These values represent the highest and lowest measured forces obtained in all acquisitions. A negative force on the hub carrier correspond to the event in which the baler's tire loses contact with the ground, meaning that at t = 75.8 s the L hub carrier registered a negative dynamic load that was approximately 3.8 times higher than the minimum static load of—1.24 kN (see Figure 4a) corresponding to the weight of one baler's wheel. The maximum and minimum loads registered by the hub carriers during this maneuver are reported again in Table 4. Furthermore, it can be noted that the time variant loads reported in Figure 15 are similar to the ones reported in Figure 12c while performing *headland turning* with the baler, also in that case, running perpendicular to the sowing lines. The higher vertical loads reported in Figure 15 in respect to the loads registered in Figure 12c can be explained by looking at the speed signals, with the baler's average speed being approximately two times higher in Figure 15 than in Figure 12c.

Figures 16 and 17 present two different portions of the signals acquired at the L and R hub carriers during *road transportation*. Figure 16 presents the overload effect of a manhole taken by the R hub carrier while running at a constant speed of approximately 20 km/h. This phenomenon causes a force range of 15.4 kN. Similarly, in Figure 17, the effect of an asphalt trench perpendicular to the road crossed at a higher speed of approximately 30 km/h is visible. In this case, a greater force range of 17.8 kN was measured on the R hub carrier.

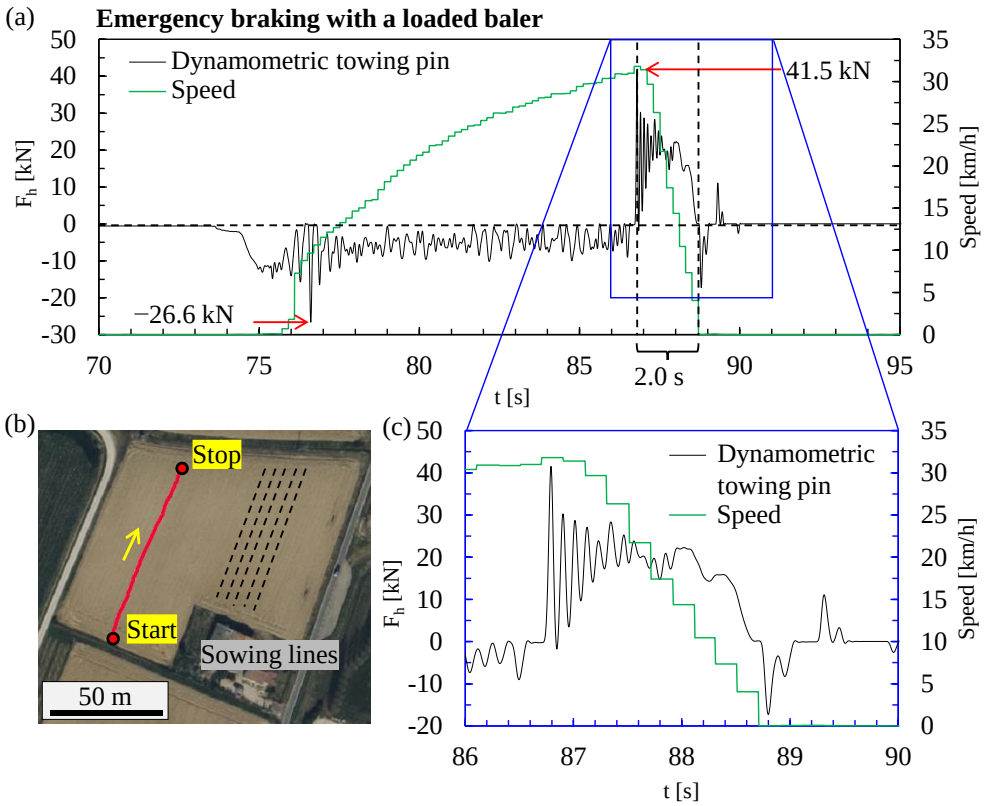

Figure 14. Horizontal loads F_h (t) registered by the dynamometric towing pin during *acceleration followed by emergency braking with a loaded baler*: (**a**,**c**) force and speed signals and (**b**) straight path followed by the baler.

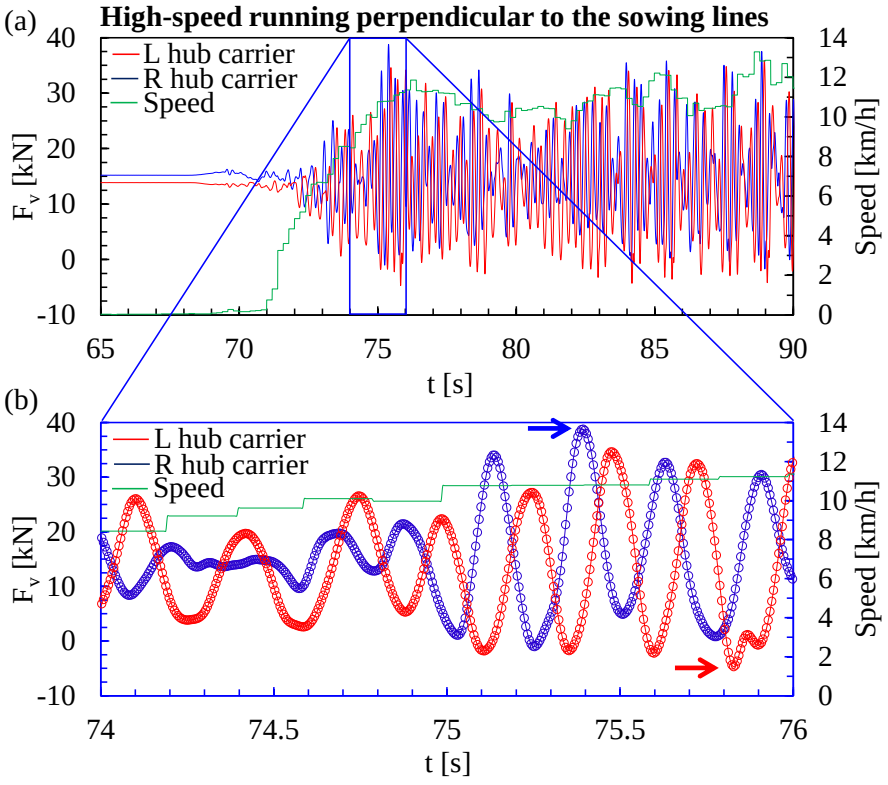

Figure 15. Vertical loads F_v(t) acting on the L and R hub carriers of the round baler during *high-speed running perpendicular to the sowing lines*: (**a**) whole force and speed signals and (**b**) details of the signals, with the maximum load $F_{v,max}$ acting on the R hub carrier and the minimum load $F_{v,min}$ acting on the L hub carrier marked by blue and red arrows, respectively.

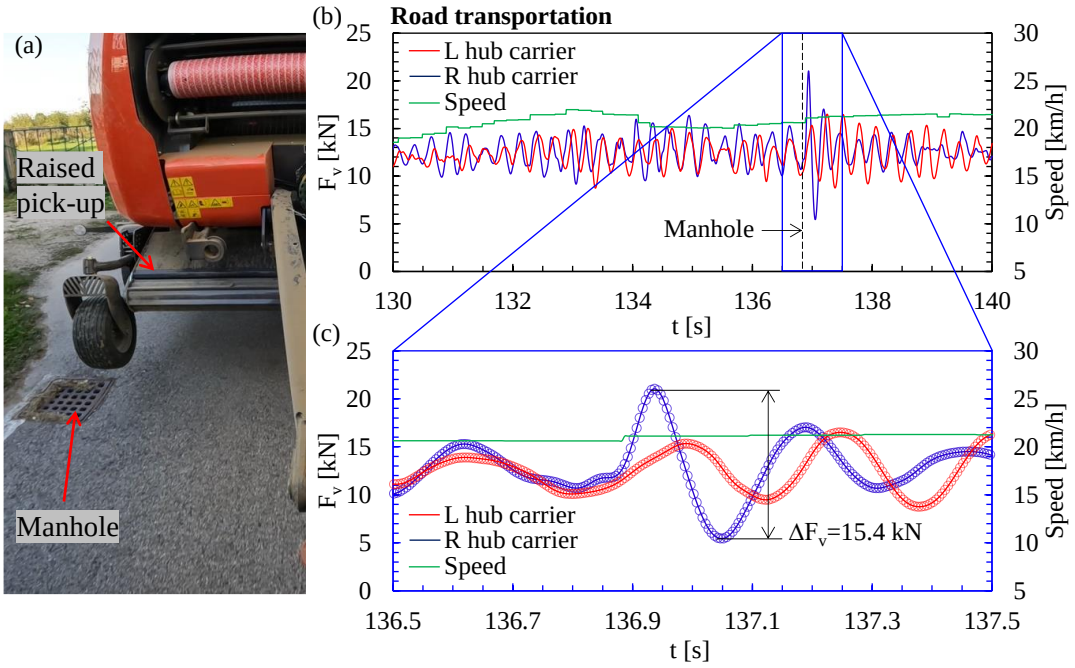

Figure 16. Effect of a manhole on the vertical loads $F_v(t)$ acting on the R hub carrier during *road transportation*: (**a**) front view of the baler with raised pick-up during *road transportation* and (**b**,**c**) details of the signals on the L and R hub carriers.

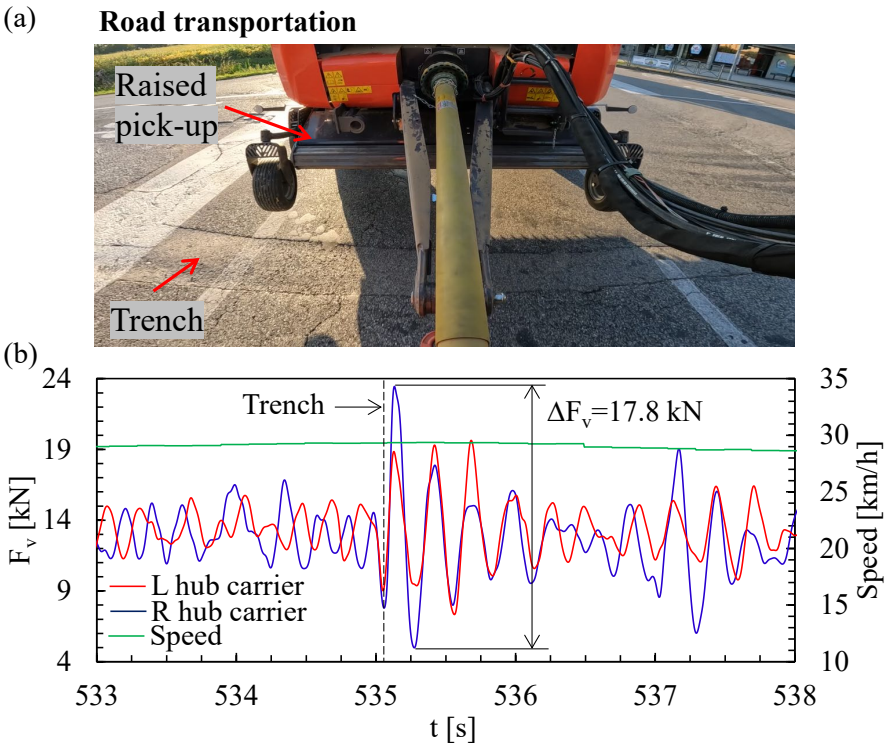

Figure 17. Effect of a road trench on the vertical loads $F_v(t)$ acting on the L and R hub carriers during *road transportation*: (**a**) front view of the baler with a raised pick-up and (**b**) details of the acquired loads on the L and R hub carriers.

Table 4 presents the maximum and minimum loads registered on the L hub carrier, R hub carrier, and the dynamometric towing pin during in-field load acquisitions.

Table 4. Maximum and minimum loads registered on the L hub carrier, R hub carrier, and dynamometric towing pin during in-field load acquisitions.

Maneuver	L Hub Carrier		R Hub Carrier		Dynamometric Towing Pin	
	$F_{v,min}$ [kN]	$F_{v,max}$ [kN]	$F_{v,min}$ [kN]	$F_{v,max}$ [kN]	$F_{h,min}$ [kN]	$F_{h,max}$ [kN]
Product collection	**7.81**	19.5	9.28	**25.0**	−8.93	7.73
Headland turning	10.3	22.0	**9.48**	**23.7**	−10.9	10.2
Acceleration followed by emergency braking with a loaded baler	**−1.20**	**33.2**	6.18	31.6	−26.6	41.5
Acceleration followed by emergency braking with an empty baler	**0.80**	25.6	3.49	**30.3**	−22.2	34.7
High-speed running perpendicular to the sowing lines	**−4.68**	35.9	−1.70	**38.8**	−33.7	29.5
Road transportation	4.66	22.6	**1.00**	**23.9**	−14.3	18.4

The maximum horizontal force $F_{h,max}$ on the dynamometric towing pin was reached during an *acceleration followed by emergency braking with a loaded baler* acquisition and resulted in +41.5 kN. Conversely, the minimum horizontal force $F_{h,min}$ was reached during *high-speed running perpendicular to the sowing lines*, where −33.7 kN was measured. The maximum and minimum vertical loads on the hub carriers, F_v, were measured during *high-speed running perpendicular to the sowing lines*, as previously mentioned. In particular, a maximum load of +38.8 kN and a minimum load of −4.68 kN were recorded on the R and L hub carriers, respectively. As previously explained while commenting on Figure 15, negative forces on the hub carrier correspond to the event in which the baler's tire loses contact with the ground.

3.2. Load Spectra

Figures 18–21 report the load spectra calculated for each channel and maneuver. Rainflow cycle counting was performed according to the ASTM E1049-85 standard using a routine available in the commercial software IMC FAMOS® 2023 Enterprise. When setting the rainflow routine, the number of classes was maintained equal to 100 in Figures 18–21. Furthermore, small range cycles and corresponding mean values were counted and unrounded (parameter three, *precise*, set to six), as recommended by IMC FAMOS® when applying the ASTM E1049-85 rainflow cycle counting algorithm. In all the rainflow graphs in Figures 18–21, the maneuver under investigation is reported along with the number of counted cycles, the number of classes, and the time window, the latter indicating the duration (expressed in seconds) of the load signals from which the rainflow was calculated. Figure 18 reports the load spectra obtained from the *product collection* maneuvers. According to Section 3.1, a distinction was made between the portions of the acquisitions when the baler was collecting product with the pick-up deployed (Figure 18a,c,e) and the portions where the baler was performing the *headland turning* with a raised pick-up (Figure 18b,d,f). Figures 19 and 20 report the load spectra obtained during *acceleration followed by emergency braking with a loaded* and *empty baler*, respectively. In this case, a distinction was made between the acceleration phase and the braking phase. Figure 21a, 21c, 21e and Figure 21b, 21d, 21f report the load spectra obtained from the *high-speed running perpendicular to the sowing lines* and from the *road transportation* maneuvers, respectively. Finally, Figure 22 reports *(i)* the recorded time mix from the in-field load acquisitions (Figure 22a), *(ii)* for each maneuver presented in Figures 18–21, the load spectra calculated at the dynamometric towing pin, R hub carrier, and L hub carrier (Figure 22b, 22d, and 22f, respectively) are represented together for better comparison, with each maneuver identified

by a different color; and *(iii)* the amplitude-only (mean values being neglected) load spectra along with their combined total (black line in Figure 22c,e,g).

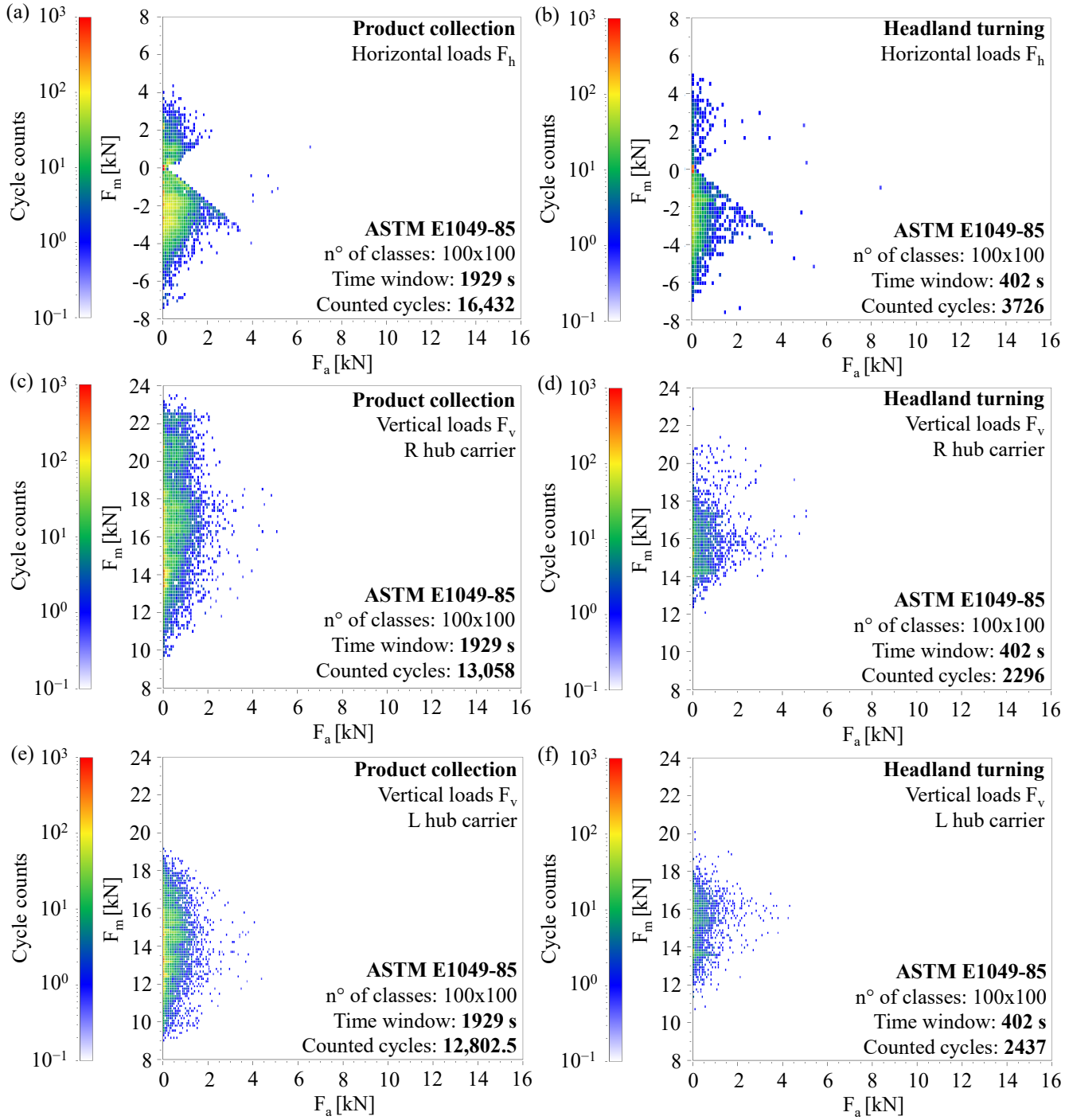

Figure 18. Load spectra calculated according to ASTM E1049-85 from the *product collection* maneuvers: (**a**,**b**) horizontal loads on the dynamometric towing pin, (**c**,**d**) vertical loads on the R hub carrier, and (**e**,**f**) vertical loads on the L hub carrier.

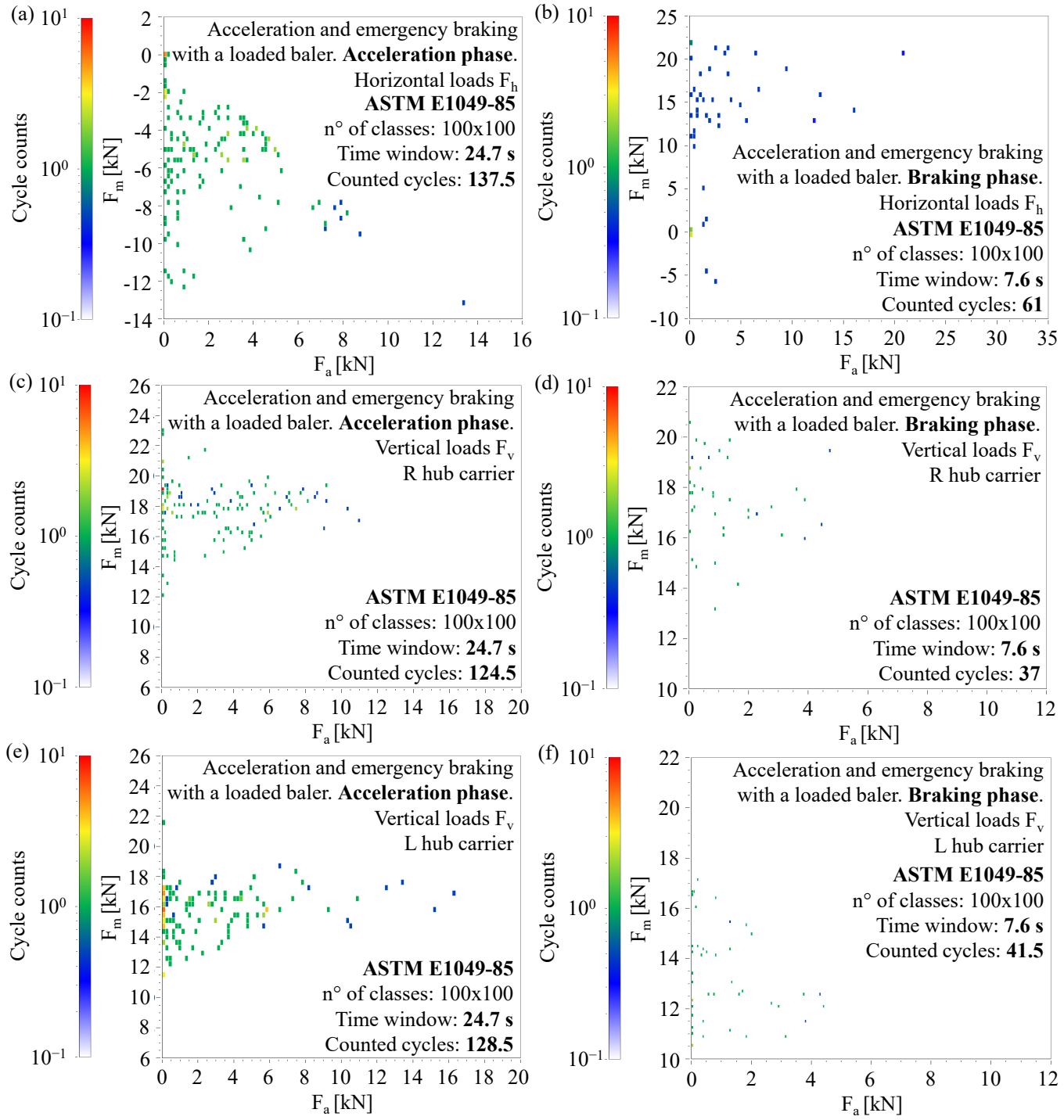

Figure 19. Load spectra calculated according to ASTM E1049-85 from the *acceleration followed by emergency braking with a loaded baler* maneuvers: (**a**,**b**) horizontal loads on the dynamometric towing pin, (**c**,**d**) vertical loads on the R hub carrier, and (**e**,**f**) vertical loads on the L hub carrier.

Dealing with the horizontal loads at the drawbar of the baler, Table 4 highlights that the highest peak load $F_{h,max}$ = 41.5 kN was registered during the *emergency braking with a loaded baler* maneuver. Differently, the highest load amplitudes were registered during the *high-speed running (at approximately 12 km/h) perpendicular to the sowing lines* maneuver with an empty baler, likely because of the highly pronounced terrain irregularities compared to the much smoother terrain irregularities during running parallel to the sowing lines. Figure 22c shows that the highest load amplitude during this maneuver is equal to 28.1 kN.

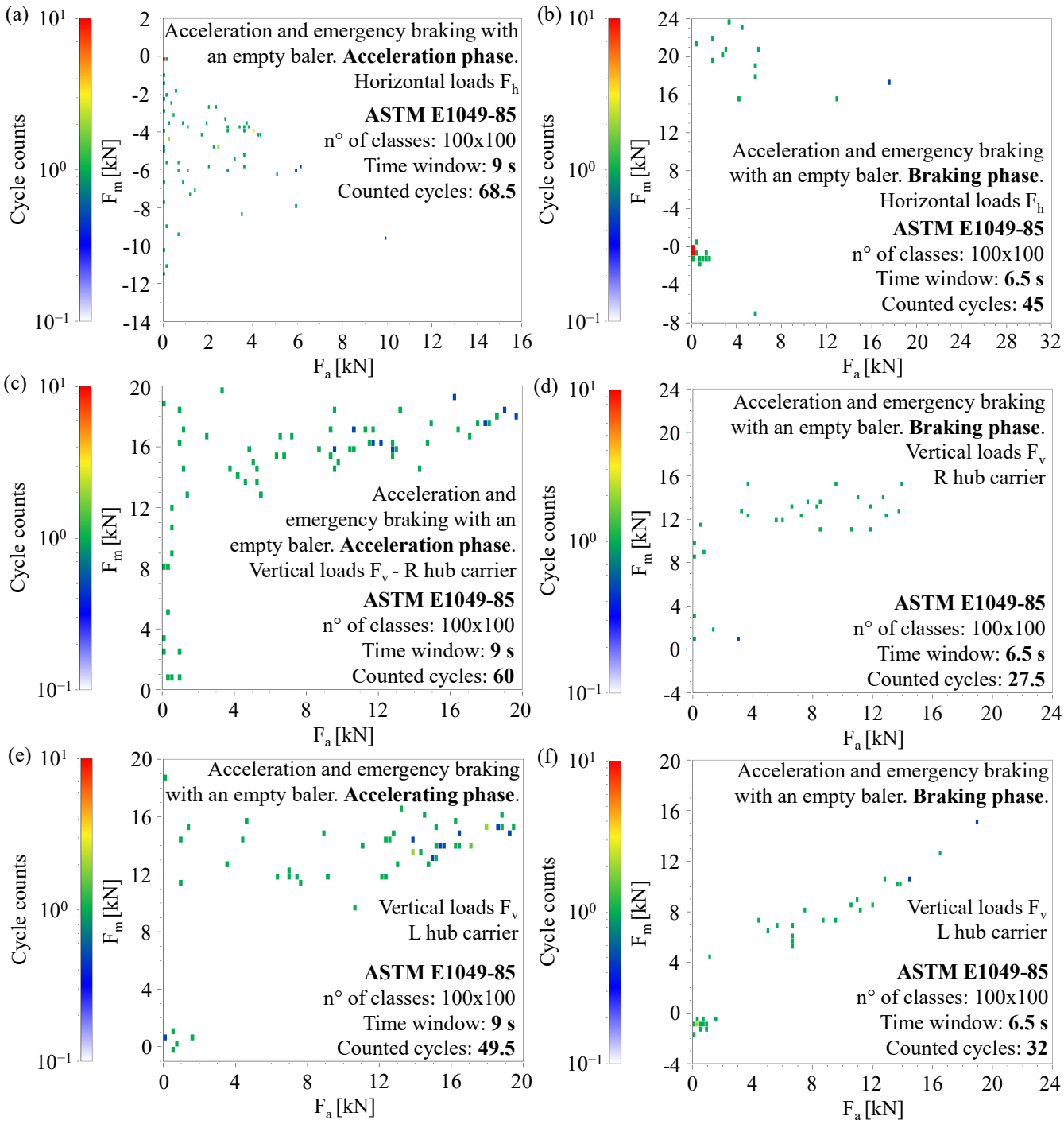

Figure 20. Load spectra calculated according to ASTM E1049-85 from the *acceleration followed by emergency braking with an empty baler* maneuver: (**a**,**b**) horizontal loads on the dynamometric towing pin, (**c**,**d**) vertical loads on the R hub carrier, and (**e**,**f**) vertical loads on the L hub carrier.

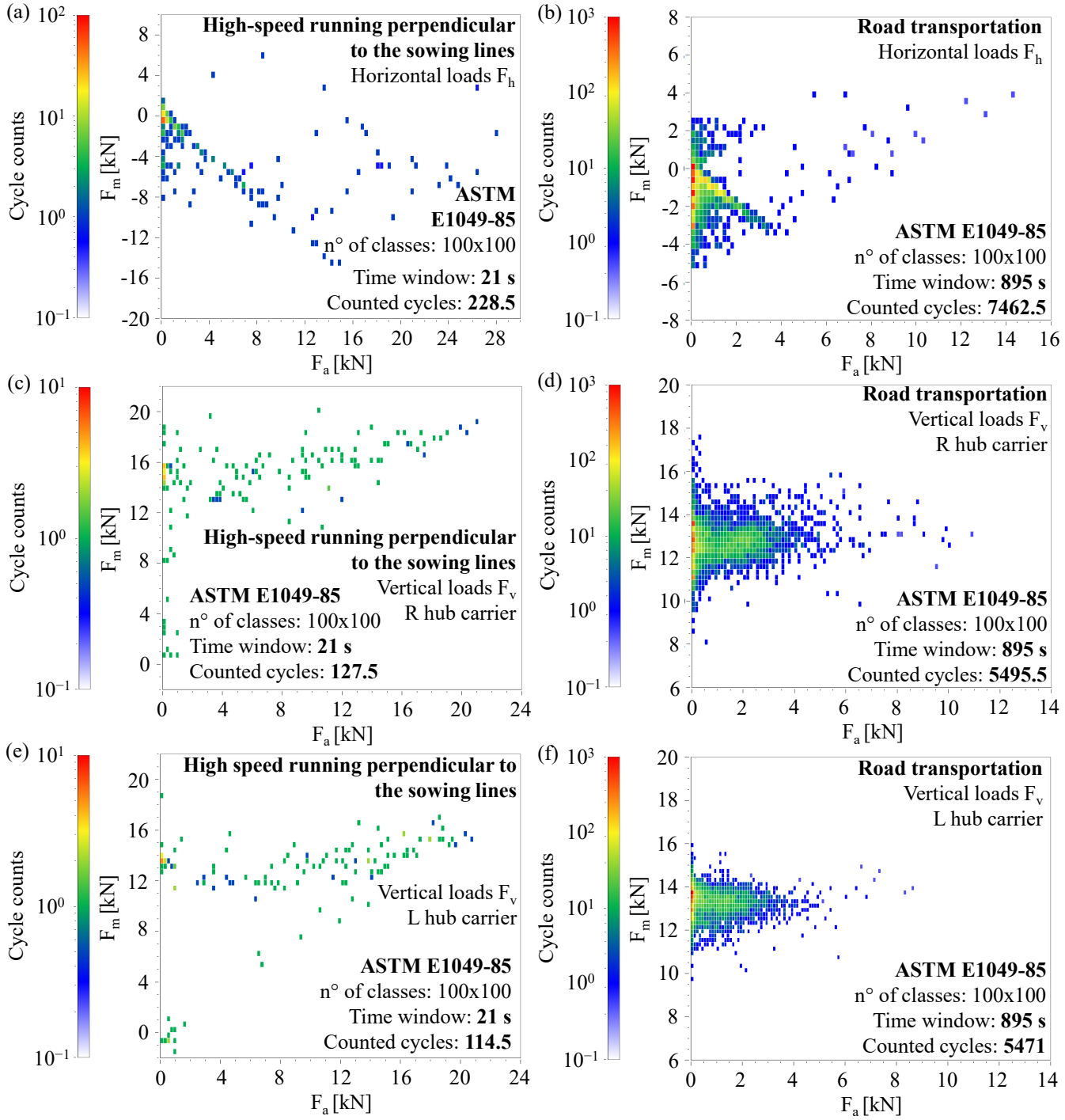

Figure 21. (**a**,**c**,**e**) Load spectra calculated according to ASTM E1049-85 from the *high-speed running perpendicular to the sowing lines* maneuver and (**b**,**d**,**f**) load spectra calculated according to ASTM E1049-85 from *road transportation*: (**a**,**b**) horizontal loads on the dynamometric towing pin, (**c**,**d**) vertical loads on the R hub carrier, and (**e**,**f**) vertical loads on the L hub carrier.

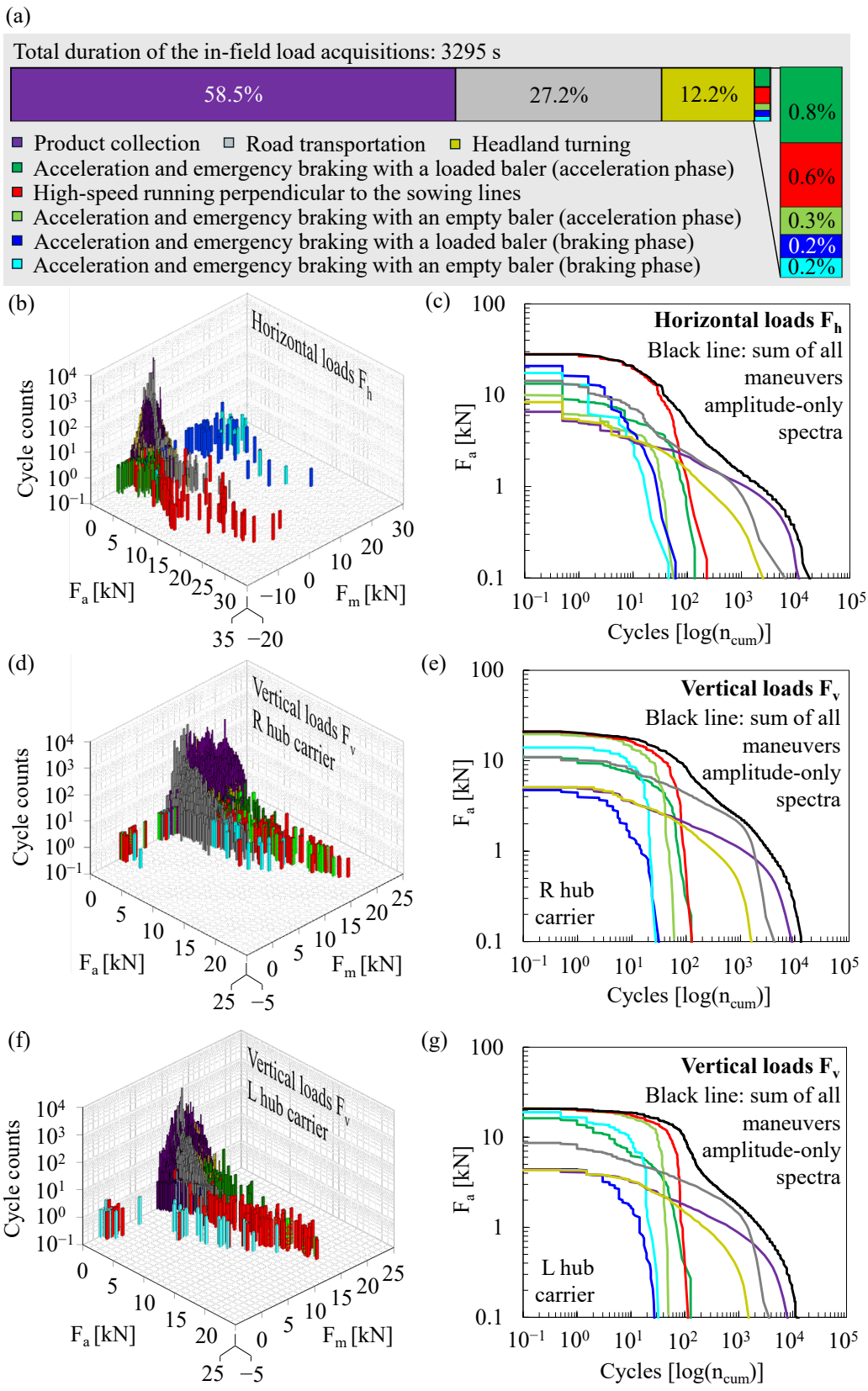

Figure 22. (**a**) Recorded time mix of the in-field load acquisition: (**b**,**d**,**f**) load spectra calculated according to ASTM E1049-85 from all maneuvers, where each maneuver is identified by a different color (see (**a**)), and (**c**,**e**,**g**) amplitude-only acquired load spectra, where each maneuver is identified by a different colour (see (**a**)). The black line is the sum of all spectra. (**b**,**c**) Horizontal loads on the dynamometric towing pin, (**d**,**e**) vertical loads on the R hub carrier, and (**f**,**g**) vertical loads on the L hub carrier.

Considering now the vertical loads at the hub carriers, both the highest peak load and load amplitude were registered at the right hub carrier during *high-speed running (at approximately 12 km/h) perpendicular to the sowing lines* with an empty baler because of the highly pronounced terrain irregularities. Specifically, Table 4 reports a peak load $F_{v,max}$ equal to 38.8 kN, while Figure 22e reports a load amplitude equal to 21.1 kN at the right hub carrier. Considering another demanding situation, namely, the higher speed of 30 km/h and smoother terrain irregularities during running parallel to the sowing lines, the second highest peak loads and load amplitudes were registered. In fact, considering the left hub carrier, a peak load $F_{v,max}$ equal to 33.2 kN was measured with a loaded baler (see Table 4) and a load amplitude equal to 19.7 kN was measured with an empty baler (see Figure 22g). These observations suggest that uneven terrain and baler speed play crucial roles in the determination of the extreme horizontal and vertical loads to which an agricultural implement may be subjected during its service life. Table 4 and Figure 22 demonstrate also that both peak loads and load amplitudes are significantly lower than the abovementioned values when the product collection maneuver is considered, due to the much lower speed (approximately between 3 and 5 km/h) the baler experiences in this case.

All previous observations suggest that uneven terrain and baler speed are the primary factors that induce the extreme horizontal and vertical loads to which the baler may be subjected during its service life.

4. Conclusions

The load spectra acting in the vertical direction on the hub carriers and in the horizontal longitudinal direction on the drawbar of a trailed variable chamber round baler were evaluated. To measure the external loads acting vertically on the hub carriers, the housings of the hub carriers were instrumented with properly calibrated strain gauge bridges. Similarly, the horizontal longitudinal loads were measured by strain gauging a dedicated towing pin. In both cases, the strain gauge channels were calibrated in the laboratory and allowed to measure the loads acting on the baler both under normal use conditions and under extreme events. The load signals were acquired during the execution of five maneuvers: *(i)* product collection, *(ii)* acceleration followed by emergency braking with the baler loaded with product, *(iii)* acceleration followed by emergency braking with the baler unloaded, *(iv)* high-speed running perpendicular to the sowing lines, and *(v)* road transportation. Moreover, the synchronous acquisition of a video via an onboard camera and a GPS signal assisted the interpretation of the acquired signals. Finally, the load spectra obtained for each maneuver were evaluated according to ASTM E1049-85. The obtained results can be summarised as follows:

- The use of instrumented hub carriers and a dynamometric towing pin allowed the measurement of external vertical and horizontal loads, respectively, during in-field load acquisitions, while maintaining the original structural components of the baler.
- The specially designed towing system equipped with a dynamometric towing pin instrumented with strain gauges was calibrated with laboratory tests and average errors lower than $\pm 6.5\%$ in the range from 10 to 40 kN were assessed.
- The maximum and minimum vertical and horizontal loads were measured during the maneuvers. As to the dynamometric towing pin, the peak horizontal load was obtained during *emergency braking with a loaded baler* and it was found to be +41.5 kN. Conversely, the peak horizontal load in the opposite direction was obtained while running at approximately 12 km/h across the sowing lines and it resulted in −33.7 kN. The maximum and minimum vertical loads on the hub carriers were recorded during the same maneuver, and the left hub carrier recorded +35.9 kN in the upward direction

and −4.68 kN in the downward direction, while the right hub carrier measured +38.8 kN and −1.70 kN. The static load component at the hub carriers with the baler configured for the *high-speed running perpendicular to the sowing lines* was found to be +14.3 kN and +13.8 kN for the left and right hub carrier, respectively.

- The load spectra obtained from approximately 3300 s of data acquisition were derived. More than 10,000 load cycles acting on the hub carriers and on the dynamometric towing pin were acquired during the product collection maneuvers. Similarly, more than 5000 load cycles were obtained during road transportation. Furthermore, the amplitude-only load spectra of each maneuver and the sum of them for the recorded time mix were calculated. The amplitude-only load spectra, to be combined with the appropriate road mix and to be extended to the target design mission, represent helpful data to guarantee the targeted mission life of the baler.

Author Contributions: Conceptualization, G.M.; methodology, G.M. and F.C.; investigation, F.C.; resources, G.M. and A.R.; data curation, G.M., A.R. and F.C.; writing—original draft preparation, F.C.; writing—review and editing, G.M., A.R. and F.C.; formal analysis, G.M.; funding acquisition, G.M. All authors have read and agreed to the published version of the manuscript.

Funding: This research was funded by UNISMART, grant number—Rep. n. 136/2023—Prot. n.2530.

Institutional Review Board Statement: Not applicable.

Informed Consent Statement: Not applicable.

Data Availability Statement: The data will be made available upon request.

Acknowledgments: Maschio Gaspardo S.p.A. is gratefully acknowledged for supporting this research.

Conflicts of Interest: Author Andrea Ruffin was employed by the company Maschio Gaspardo S.p.A. The remaining authors declare that the research was conducted in the absence of any commercial or financial relationships that could be construed as a potential conflict of interest.

References

1. Rushton, A.; Croucher, P.; Baker, P. *The Handbook of Logistics and Distribution Management*, 7th ed.; Kogan Page: London, UK, 2010.
2. Kovács, G. Optimization Method and Software for Fuel Cost Reduction in Case of Road Transport Activity. *Acta Polytech.* **2017**, *57*, 201–208. [CrossRef]
3. Gao, T.; Erokhin, V.; Arskiy, A. Dynamic Optimization of Fuel and Logistics Costs as a Tool in Pursuing Economic Sustainability of a Farm. *Sustainability* **2019**, *11*, 5463. [CrossRef]
4. Larson, L.W. Predicting Draft Forces Using Model Moldboard, Plows in Agricultural Soils. Retrospective Theses and Dissertations. Ph.D. Thesis, Iowa State University of Science and Technology, Ames, IA, USA, 1964.
5. Decker, M.; Savaidis, G. Measurement and Analysis of Wheel Loads for Design and Fatigue Evaluation of Vehicle Chassis Components. *Fatigue Fract. Eng. Mater. Struct.* **2002**, *25*, 1103–1119. [CrossRef]
6. Armin, A. Mechanics of Soil-Blade Interaction. Ph.D. Thesis, University of Saskatchewan, Saskatoon, SK, Canada, 2014.
7. Malón, H.; Aguirre, A.; Boné, A.; Vidal, M.; García-Ramos, F. Design and Testing of an Agricultural Implement for Underground Application of Rodenticide Bait. *Sensors* **2015**, *15*, 2006–2020. [CrossRef] [PubMed]
8. Al-Neama, A.K.A.; Herlitzius, T. Draft Forces Prediction Model for Standard Single Tines by Using Principles of Soil Mechanics and Soil Profile Evaluation. *Landtechnik* **2017**, *72*, 157–164.
9. Thomson, N.P.; Shinners, K.J. A Portable Instrumentation System for Measuring Draft and Speed. *Appl. Eng. Agric.* **1989**, *5*, 133–137. [CrossRef]
10. Watyotha, C.; Salokhe, V.M. Development of a Data Acquisition System for Measuring the Characteristics of Real Time Forces by Cage Wheels. *J. Terramech.* **2001**, *38*, 201–210. [CrossRef]
11. Foster, J.D.G. Measurement of Central or Offset Axle Load by Axle-Mounted Strain Gauges. *Strain* **2003**, *39*, 21–26. [CrossRef]
12. McCarthy, M.A.; Lawlor, V.P.; O'Donnell, P.C.; Harris, K.; Kelly, P.; Cunningham, J.P. Measurement of Bolt Pre-Load in Torqued Composite Joints. *Strain* **2005**, *41*, 109–112. [CrossRef]
13. Olmi, G.; Freddi, A.; Croccolo, D. In-Field Measurement of Forces and Deformations at the Rear End of a Motorcycle and Structural Optimisation: Experimental-Numerical Approach Aimed at Structural Optimisation. *Strain* **2008**, *44*, 453–461. [CrossRef]

14. Näsellqvist, M.; Gustavsson, R.; Aidanpää, J.-O. Bearing Load Measurement in a Hydropower Unit Using Strain Gauges Installed Inside Pivot Pin. *Exp. Mech.* **2012**, *52*, 361–369. [CrossRef]
15. Paraforos, D.S.; Griepentrog, H.W.; Vougioukas, S.G.; Kortenbruck, D. Fatigue Life Assessment of a Four-Rotor Swather Based on Rainflow Cycle Counting. *Biosyst. Eng.* **2014**, *127*, 1–10. [CrossRef]
16. Bai, J.; Wu, X.; Gao, F.; Li, H. Analysis of Powertrain Loading Dynamic Characteristics and the Effects on Fatigue Damage. *Appl. Sci.* **2017**, *7*, 1027. [CrossRef]
17. Jie, Z.; Miao, Z.; Ming, C. Design and Experiment of an On-the-Go Soil Mechanical Resistance System. *IFAC-PapersOnLine* **2018**, *51*, 199–205. [CrossRef]
18. Petrone, N.; Meneghetti, G. Fatigue Life Prediction of Lightweight Electric Moped Frames after Field Load Spectra Collection and Constant Amplitude Fatigue Bench Tests. *Int. J. Fatigue* **2019**, *127*, 564–575. [CrossRef]
19. Cardei, P.; Matache, M.; Persu, C.; Sfiru, R.; Muraru, S.; Cristea, M. Simulation of the Calibration Process of the Strain Gauge Measurement Systems. In Proceedings of the 2021 13th International Conference on Electronics, Computers and Artificial Intelligence (ECAI), Pitesti, Romania, 1–3 July 2021; IEEE: Piscataway, NJ, USA, 2021; pp. 1–7.
20. Santana, L.; Rivera, D.; Forcael, E. Force Measurement with a Strain Gauge Subjected to Pure Bending in the Fluid–Wall Interaction of Open Water Channels. *Appl. Sci.* **2022**, *12*, 1744. [CrossRef]
21. Correia, A.; Manuel, A.; Jesus, P.D.; Maruschak, P.; Qian, G.; Pástor, M.; Lengvarský, P.; Hagara, M.; Kul'ka, J. Experimental Investigation of the Fatigue Life of a Bridge Crane Girder Using S-N Method. *Appl. Sci.* **2022**, *12*, 10319. [CrossRef]
22. Pástor, M.; Hagara, M.; Gašpár, Š.; Sapieta, M. Design and Implementation of a Low-Cost Torque Sensor for Manipulators. *Appl. Sci.* **2023**, *13*, 9406. [CrossRef]
23. Celik, H.K.; Akinci, I.; Caglayan, N.; Rennie, A.E.W. Structural Strength Analysis of a Rotary Drum Mower in Transportation Position. *Appl. Sci.* **2023**, *13*, 11338. [CrossRef]
24. Gür, Y.; Cen, G. Comparison of Finite Element Analysis Results with Strain Gauge Measurements of a Front Axle Housing. *Mech. Sci.* **2024**, *15*, 257–268. [CrossRef]
25. Szusta, J.; Derpeński, Ł.; Karakaş, Ö.; Tüzün, N.; Dobrzański, S. Effect of Welding Process Parameters on the Strength of Dissimilar Joints of S355 and Strenx 700 Steels Used in the Manufacture of Agricultural Machinery. *Materials* **2023**, *16*, 6963. [CrossRef] [PubMed]
26. Khan, J.; Godwin, R.J.; Kilgour, J.; Blackmore, B.S. Design and Calibration of a Direct Mounted Strain Gauged Lower Links System for Measurement of Tractor-Implement Forces. *ARPN J. Eng. Appl. Sci.* **2006**, *1*, 22–25.
27. Kostić, M.M.; Rakić, D.Z.; Ličen, H.H.; Malinović, N.C. Design and Construction of Three Point Hitch Device for Measuring Draft of Tillage Implement—Data Acquisition and Post Processing Analysis. *J. Food Agric. Environ.* **2014**, *12*, 1300–1307.
28. Yang, Z.; Wang, S.; Wang, Q.; Xie, Y. Three-Dimensional Bearing Load Sensor Design and Numerical Investigations. *Sens. Actuators A Phys.* **2007**, *136*, 304–312. [CrossRef]
29. Rasolofondraibe, L.; Pottier, B.; Marconnet, P.; Chiementin, X. Capacitive Sensor Device for Measuring Loads on Bearings. *IEEE Sens. J.* **2012**, *12*, 2186–2191. [CrossRef]
30. Hensh, S.; Tewari, V.K.; Upadhyay, G. An Instrumentation System to Measure the Loads Acting on the Tractor PTO Bearing during Rotary Tillage. *J. Terramech.* **2021**, *96*, 1–10. [CrossRef]
31. O'Dogherty, M.J. The Design of Octagonal Ring Dynamometers. *J. Agric. Eng. Res.* **1996**, *63*, 9–18. [CrossRef]
32. Lee, D.-H.; Kim, Y.-J.; Chung, S.-O.; Choi, C.-H.; Lee, K.-H.; Shin, B.-S. Analysis of the PTO Load of a 75 kW Agricultural Tractor during Rotary Tillage and Baler Operation in Korean Upland Fields. *J. Terramech.* **2015**, *60*, 75–83. [CrossRef]
33. Kim, Y.-J.; Chung, S.-O.; Choi, C.-H. Effects of Gear Selection of an Agricultural Tractor on Transmission and PTO Load during Rotary Tillage. *Soil Tillage Res.* **2013**, *134*, 90–96. [CrossRef]
34. Kim, Y.S.; Kim, W.S.; Baek, S.Y.; Baek, S.M.; Kim, Y.J.; Lee, S.D.; Kim, Y.J. Analysis of Tillage Depth and Gear Selection for Mechanical Load and Fuel Efficiency of an Agricultural Tractor Using an Agricultural Field Measuring System. *Sensors* **2020**, *20*, 2450. [CrossRef]
35. Shao, Y.; Liu, J.; Mechefske, C.K. Drive Axle Housing Failure Analysis of a Mining Dump Truck Based on the Load Spectrum. *Eng. Fail. Anal.* **2011**, *18*, 1049–1057. [CrossRef]
36. Palmgren, A. Die Lev/Bensdauer von Kugellagern. *VDI Z.* **1924**, *68*, 339–341.
37. Miner, M. Cumulative Damage in Fatigue. *J. Appl. Mech.* **1945**, *67*, A159–A164. [CrossRef]
38. Sonsino, C.M.; Łagoda, T.; Demofonti, G. Damage Accumulation under Variable Amplitude Loading of Welded Medium- and High-Strength Steels. *Int. J. Fatigue* **2004**, *26*, 487–495. [CrossRef]
39. Molent, L.; Aktepe, B. Review of Fatigue Monitoring of Agile Military Aircraft. *Fatigue Fract. Eng. Mater. Struct.* **2000**, *23*, 767–785. [CrossRef]
40. Maglio, M.; Kabo, E.; Ekberg, A. Railway Wheelset Fatigue Life Estimation Based on Field Tests. *Fatigue Fract. Eng. Mater. Struct.* **2022**, *45*, 2443–2456. [CrossRef]

41. Dong, Q.; Xu, G.N.; Ren, H.L.; Wang, A.H. Fatigue Remaining Life Estimation for Remanufacturing Truck Crane Jib Structure Based on Random Load Spectrum. *Fatigue Fract. Eng. Mater. Struct.* **2017**, *40*, 706–731. [CrossRef]
42. Wang, Q.; Zhou, J.; Wang, T.; Gong, D.; Sun, Y.; Chen, J.; You, T. Extrapolation of the Dynamic Stress Spectrum of Train Bogie Frame Based on Kernel Density Estimation Method. *Fatigue Fract. Eng. Mater. Struct.* **2021**, *44*, 1783–1798. [CrossRef]
43. *ASTM E1049-85*; Standard Practices for Cycle Counting in Fatigue Analysis. ASTM International: West Conshohocken, PA, USA, 2017.
44. HBM Prewired Strain Gauges. 2024. Available online: https://www.hbm.com/en/4550/pre-wired-strain-gauges-fast-safe-and-convenient/?product_type_no=Prewired%20Strain%20Gauges/ (accessed on 31 October 2024).
45. Doebelin, D.N.; Ernest, O. *Measurement Systems: Application and Design*; Tata McGraw Hill: New Delhi, India, 2007.
46. Coppola, F.; Mariotto, M.; Pagnin, L.; Peraro, R.; Spigolon, S.; Battistello, A.; Brazzoli, L.; Ruffin, A.; Meneghetti, G. Development of Methods to Acquire the In-Field Load Spectra Acting on a Variable Chamber Round Baler. In Proceedings of the 53rd AIAS National Conference (In Italian), Naples, Italy, 4–7 September 2024.
47. *EN 1993-1-1*; Eurocode No. 3: Design of Steel Structures. Part 1.1: General Rules and Rules for Buildings. CEN: Brussels, Belgium, 2005.
48. Hobbacher, A.F. *Recommendations for Fatigue Design of Welded Joints and Components*; IIW Collection; Springer International Publishing: Berlin/Heidelberg, Germany, 2024. [CrossRef]
49. Kyowa General-Purpose Foil Strain Gages. 2024. Available online: https://product.kyowa-ei.com/en/products/strain-gages/type-kfgs/ (accessed on 31 October 2024).